arXiv:astro-ph/0008242v1 16 Aug 2000

Near-Infrared Spectroscopy of Two Galaxies at $z = 2.3$ and $z = 2.9$: New Probes of Chemical and Dynamical Evolution at High Redshift[1]

Henry A. Kobulnicky[2]

Astronomy Department, University of Wisconsin - Madison

475 N. Charter St., Madison, WI 53706

chip@astro.wisc.edu

David Koo

UCO/Lick Observatory

Department of Astronomy and Astrophysics

University of California, Santa Cruz

Santa Cruz, CA 95064

koo@ucolick.org

Final Draft of 2000 August 15

ABSTRACT

This study presents Keck optical and infrared spectroscopy of the rest-frame ultraviolet and optical emission lines in two Lyman α emitting galaxies at $z > 2$. These data provide insight on the evolution of fundamental galaxy scaling relations at early epochs, especially the luminosity-velocity and luminosity-metallicity relations. Spectral diagnostics suggest that the Coup Fourré Galaxy at $z = 2.3$ [CFg; Lowenthal et al. 1991] and Lynx 2-9691, a serendipitously-discovered, luminous Lyman-drop galaxy at $z = 2.9$, are star-forming galaxies without active nuclei. Lynx 2-9691 exhibits extended [O III] emission over a diameter of >28 kpc, reminiscent of the Lyman α nebulae discovered near Lyman-drop galaxies [Steidel et al. 2000]. We estimate star formation rates of 59 $M_\odot\ yr^{-1}$ and 111 $M_\odot\ yr^{-1}$, respectively, from Balmer recombination line luminosities, 2-3 times higher than inferred from the ultraviolet continuum. The ratios of strong nebular emission lines indicate sub-solar oxygen abundances in the range $8.2 < 12 + log(O/H) < 8.8$ ($Z = 0.25 - 0.95\ Z_\odot$). Interestingly, Galactic metal-rich

[1]Based on observations obtained at the W. M. Keck Observatory which is operated jointly by the University of California and the California Institute of Technology.

[2]Hubble Fellow

globular clusters have similar metallicities, consistent with the idea that we could be seeing the formation of galaxies like the Milky Way at $z \sim 3$. The measured gas phase oxygen abundances are $> 4-10$ times higher than the $Z < 0.1 Z_{\odot}$ metallicities found in damped Lyman α (DLA) absorbers at similar redshifts, indicating that DLA systems trace fundamentally different environments than the vigorously star-forming objects observed here. If this intense star formation activity represents the dominant formation episodes for stars in today's spiral bulges or ellipticals, then the evolved descendants in the local universe should exhibit similarly sub-solar metallicities in their dominant stellar populations which formed 8-10 Gyr ago. When these new data are combined with a sample of four other high-redshift spectroscopic results from the literature, we find that star-forming galaxies at $z \sim 3$ are 2-4 magnitudes more luminous than local spiral galaxies of similar metallicity, and thus, are offset from the local luminosity-metallicity relation. Their kinematic linewidths are $\sigma_v = 65 - 130$ km s^{-1}, making this sample 1-3 magnitudes more luminous than local galaxies of similar linewidth and mass. Less luminous Lyman-drop galaxies need to be studied to see if these deviations are universal or apply to only the most luminous high-redshift galaxies.

Subject headings: galaxies: formation — galaxies: evolution — galaxies: fundamental parameters — galaxies: abundances — Galaxy: abundances — Galaxy: globular clusters

1. Introduction

The early epochs of galaxy formation have recently become accessible to direct observation (see reviews by Dickinson 2000; Steidel 1999; Stern & Spinrad 1999). Of particular importance are the so-called "Lyman drop" galaxies[3] at redshifts $z > 2$ with high star formation rates suggesting that they may be the progenitors (Steidel et al. 1996a,b) or building blocks (Lowenthal 1997) of today's ellipticals, spiral bulges, and spiral halos. Virial masses determined from the optical emission linewidths have lower limits of a few$\times 10^{10}$ $M_{\odot}$. Balmer line luminosities indicate star formation rates (SFR) of 20-270 $M_{\odot}\ yr^{-1}$, a factor of several times higher than the SFR implied from their ultraviolet continuum luminosities (Pettini et al. 1998). During this period 8-10 Gyr ago, it appears that many of today's large cluster galaxies and the universe as a whole (Madau et al. 1996, Steidel et al. 1999) were undergoing their dominant episodes of star formation.

Infrared spectroscopy in the near-IR windows provides a view of the rest-frame optical properties of galaxies in this active redshift range, $2.0 < z < 3.5$. One application has been the de-

[3]We prefer to use the term "Lyman-drop" instead of "Lyman break" since the intergalactic Lyman α forest absorption, and not just the Lyman break at 912 Å may also contribute to a decrease in the far UV flux, especially at higher redshifts. See Lowenthal et al. 1997 where this is demonstrated empirically by the use of B-band in addition to U-band dropouts to select $z \sim 2.5$ galaxies.

termination of gas-phase metallicities within galaxies over the same redshift ranges where damped Lyman α (DLA) systems show metallicities $\leq 0.1\ Z_{\odot}$ (Pettini et al. 1997a,b;1999; Lu et al. 1996). DLA systems show little or no change in metallicity from $z = 3$ to the present (Prochaska & Wolf 1999, 2000; Pettini et al. 1999), in conflict with theoretical expectations (Pei, Fall, & Hauser 1999, although see Cen & Ostriker 1999). Another application is to understand how fundamental galaxy parameters like size, mass, luminosity, and metallicity scale when the universe was just 10% its present age and galaxies were in their youth.

These types of studies are only beginning with the advent of near-IR spectrographs on 8-10 m class telescopes. Teplitz (2000a,b) presented infrared spectra of strong nebular lines in two $z > 3$ Lyman-drop galaxies. They derived slightly sub-solar gas-phase metallicities in the range 0.2-0.9 $Z_{\odot}$ and star formation rates several times higher than those inferred from the ultraviolet continuum luminosities. In this paper we report optical and infrared spectroscopy for two additional objects at $z > 2.3$: Lynx 2-9691, a serendipitously-discovered luminous Lyman-drop galaxy and another Lyman α emission galaxy known as the "Coup Fourré Galaxy" (CFg; Lowenthal et al. 1991; Roche, Lowenthal, & Woodgate 2000). In all luminosity-related computations, we assume a cosmology with $H_0 = 70\ km\ s^{-1}\ Mpc^{-1}$, $\Omega_0 = 0.2$, and $\Omega_{\Lambda} = 0$.[4]

2. Data Acquisition

The two high-redshift objects were observed in the optical and infrared spectral regions at the Keck II telescope. Using the NIRSPEC infrared spectrograph (McLean et al. 2000) during UT 2000 January 23–24, we obtained spectra of Lynx 2-9691 and the CFg. Table 1 lists positions, redshifts, and apparent magnitudes for the two target objects.

The CFg was discovered as a strong Lyman α emitter $48''$ from QSO PHL 957, which possesses a damped Lyman α system at the same redshift. The CFg has a redshift of $z = 2.3128$ (Lowenthal et al. 1991) and is composed of two components, CFgA and CFgB, separated by $0.35''$. For our purposes, we consider both components together as a single galaxy. Lynx 2-9691 was discovered serendipitously during a Keck study of the chemical compositions of $z \sim 0.4$ galaxies in the Lynx 2 field (Kobulnicky & Zaritsky 1999). During an optical observing run with the LRIS spectrograph (Oke 1995) on Keck II during 1997 November, we obtained the discovery spectrum of Lynx 2-9691 over the wavelength range 3650 Å– 8000 Å. Details of the observations and reductions are given in Kobulnicky & Zaritsky (1999). The spectrum has a resolution of 9 Å FWHM, an integration time of 1.5 hours, and is flux calibrated based on spectrophotometric standards. Lynx 2-9691 appears as a star-like object near the limit of $R_F \simeq 23$ on deep 4-m photographic plates and lies at $z = 2.8877$. Figure 1a shows a $37''$ image of the field from scans of photographic plates (M. Bershady, private communication) taken with the R_F filter (Kron 1980). Rectangles mark the

[4]Adopting instead a flat $\Omega_{\Lambda} = 0.7$ cosmology would change the derived luminosities by <0.2 mag. at $z = 3$.

positions of Keck LRIS slitlet used in the discovery observations and the Keck/NIRSPEC slit used for IR spectroscopy. Figure 1b shows the 2-D Keck/LRIS discovery spectrum of Lynx 2-9691. Strong Lyman α emission is seen near $z = 2.9$. With an observed magnitude of $R_F \sim 23$ (Table 1), it is among the most luminous Lyman-drop galaxies when compared to the sample of Steidel et al. (1996, 1998). Lynx 2-9691, however, may be lensed, since it lies within a few arcsec of several other faint galaxies, including an early type galaxy, Lynx 2-9689, located 3.5″ to the NE, which shows strong stellar Ca H&K absorption features at $z = 0.31$. High-quality imaging of the field and measured redshifts for the other field galaxies would be useful to address this possibility. Unless otherwise noted, we assume that there is no magnification due to lensing. In any case, lensing will not change the measured chemical composition or kinematic linewidth, only the apparent luminosity and size of the system.

We obtained low resolution $R \simeq 1300$ spectra of each object in three near-infrared passbands selected to contain the redshifted emission lines of [O II] λ3727, Hβ, [O III] λ5007, and Hα. In the case of the CFg, these passbands correspond to the standard *JHK* filters. For Lynx 2-9691, the NIRSPEC N4, N6, and N7 filters were used. The position angle of the slit was 46 degrees for the CFg observations and 118 degrees for Lynx 2-9691. Table 2 summarizes the wavelength coverage, integration times, and other relevant observational details. Between two and five exposures measuring 300 s to 900 s were obtained of each object. Airmasses ranged between 1.11 and 1.55. In all cases, the 42″x 0.76″ longslit, the widest available, was used. The scale of the 1024x1024 detector is 0.178″/pix in the spatial direction and 0.14″/pix in the spectral direction. Between exposures, the telescope was dithered (i.e., repositioned) to move the object several arcseconds along the slit. Seeing varied between 0.6″and 1.1″. Both nights were clear, but windy.

2.1. Reductions and Calibration

The NIRSPEC data reduction in IRAF[5] involved division by a halogen lamp flat field to remove pixel sensitivity variations in the spectral direction. To remove the strong night sky emission lines and background, we subtracted from each frame the dithered frame immediately preceding or following each exposure. Wavelength calibration was performed using the OH airglow lines present in each frame. The wavelength solution was good to an RMS of 2 Å. The output pixel scale was ~ 3 Å/pix. Gaussian fits to individual night sky lines indicate a mean spectral resolution of 13 Å FWHM at 1.6 μm or $R \sim 1250$. Observations of the twilight sky were used to correct the spectra for response variations along the slit. In practice, all objects were observed within 10″ of the slit center where the response is uniform.

Spectra were aligned spatially by shifting an integer number of pixels along the slit. In most

[5]IRAF is distributed by the National Optical Astronomy Observatories, which are operated by the Association of Universities for Research in Astronomy, Inc., under cooperative agreement with the National Science Foundation.

cases, offsets were determined directly from emission lines visible in the individual background-subtracted frames. No continuum from the target galaxies was detected. When no emission lines were present, offsets were determined from stars in the slit viewing camera (SCAM) images. Similar images were combined by averaging with rejection for cosmic rays. Spectral extraction was accomplished with the aid of spatial traces from standard star exposures.

Flux calibration is based upon observations of the spectrophotometric standard star Feige 34 (Oke 1990) observed at airmass 1.40 and of a V=10.02 K4V star, HIP 23694 (≡GSC 03734-00980), observed at airmass 1.20. We obtained the absolute flux calibration of Feige 34 using the the STScI STIS/NICMOS optical calibration of hot white dwarfs (see Bohlin 2000; Bohlin 1996) and modeling Feige 34 as a blackbody of temperature 67,000 K (Thejll, Ulla, & MacDonald 1995) to extrapolate from the optical into the infrared bands. This approach was adopted after comparing model blackbody curves to the optical and infrared observations of another similarly hot white dwarf, G191B2b. This approach, however, neglects the small amplitude Bracket absorption lines in the atmosphere of the white dwarf. Fortunately, these absorption lines do not fall at the wavelengths where we are calibrating emission lines in the high-redshift targets, so there is no impact on the flux calibration. For HIP 23694, we use the spectral energy distribution of a K4V star (Pickles 1988) and normalize the flux using V=10.02 (Hipparchos Catalog). Thus, we have two independent flux calibrations which agreed to within 10% over the range of bandpasses used here. For each star, we used the ratio of the model to the observed spectrum to produce a flux calibration curve which converts raw count rates into flux calibrated spectra. This correction factor implicitly includes the corrections for instrumental response as a function of wavelength, as well as atmospheric transmission effects *at one particular airmass.* Because atmospheric opacity changes with airmass, there will be small residuals in the flux calibration for spectral regions with large opacity. Since the standard star observations bracket the range of airmasses for the targets, these residual factors should be small.

In summary, the *relative* flux calibration *within* a given bandpass appears to be good to a few percent in regions uncontaminated by night sky emission lines or atmospheric absorption features. The relative calibration *across bandpasses* is accurate to about 15%. The zero point of the flux calibration may overestimate the flux of the targets due to slit losses during observation of the standard stars. However, slit losses during target observations will work in the opposite direction to reduce, or even underestimate, the flux of sources. The seeing averaged 0.6-1.1″ while the maximum slit width for NIRSPEC in longslit mode is 0.76″. Since we are primarily interested in the *relative* flux between one spectral line and another, the calibration is adequate for the present purposes.

3. Results and Analysis

The extracted spectra of the targets appear in Figures 2–8. Figure 2 is the optical (rest-frame ultraviolet) spectrum of CFg, from Lowenthal et al. (1991). The prominent Lyman α line

is marked along with He II λ1640 and C IV λ1549. A sample night sky spectrum appears below, scaled arbitrarily, for reference purposes. Lowenthal et al. (1991) argue that this is a normal star-forming galaxy, rather than an AGN, on the basis of the small velocity width (<700 km s^{-1}) and lack of high ionization lines like N V λ1240 normally seen in Seyfert galaxies. High resolution HST imaging shows no evidence of a central point source that would indicate nuclear activity (Roche et al. 2000). However, the presence of He II λ 1640 and C IV λ1549 in emission suggest a high degree of ionization seen only in the most energetic star formation regions.

Figure 3 shows the optical (rest-frame ultraviolet) spectrum of Lynx 2-9691 from rest wavelengths 950 Å–2050 Å. Night sky airglow lines appear below, scaled arbitrarily. The expected positions of common nebular emission and absorption lines are marked. Most prominent is Lyman α with a rest-frame equivalent width of 18 Å. The reported equivalent widths are corrected to the rest frame using

$$EW_{rest} = EW_{observed}/(1+z). \quad (1)$$

He II λ1640 is present in emission, and possibly C III] λ1909. If so, both are indicators of a high ionization level, probably due to massive stars. The most prominent absorption features are C IV λ1548/51 and Si IV λ1394/1403. These may have either interstellar or stellar origins.

Figure 4 shows an expanded portion of the Lynx 2 spectrum in the far ultraviolet. Nearly all of the observed features are common in atmospheres of O and Wolf-Rayet stars seen with IUE (Neubig & Bruhweiler 1999) and the Hopkins Ultraviolet Telescope (Schulte-Ladbeck, Hillier, & Herald 1995). The presence of these strong stellar/interstellar features, and the absence of broad, high-ionization features is consistent with normal star-forming galaxies containing massive stars. The spectra in Figures 3 and 4 bear many similarities to the Lyman-drop galaxies, argued to be normal star-forming galaxies by Steidel et al. (1996a,b).

Figure 5 shows the sky-subtracted 2-D spectra for the CFg. Positions of the strong nebular lines are labeled. Figure 6 shows the extracted 1-D infrared J, H, K band spectra of CFg. Night sky emission lines appear below each target spectrum, scaled arbitrarily. An atmospheric transmissivity curve based on models for Mauna Kea (Lord 1992) is plotted above each spectrum, scaled arbitrarily, with a horizontal scale bar indicating zero transmissivity. These curves serve to show that the major emission lines are not strongly affected by regions of atmospheric absorption. Marks denote the expected redshifted positions of [O II] λ3727, Hβ, [O III] $\lambda\lambda$4959/5007, and Hα. [O III] λ5007 and Hα are clearly detected, while [O III] λ4959 is a less certain detection due to contamination by neighboring OH airglow lines. [N II] λ6584 is not detected as it falls at the position of a strong night sky line just redward of $H\alpha$. Hβ is not detected, even though it falls in between strong night sky lines. $H\beta$ is susceptible to absorption by the underlying stellar population, an effect which may contribute to its non-detection. [O II] λ3727 lies in a region contaminated by sky lines, and is not unambiguously detected. No continuum is present in any of the infrared spectra. Extrapolating the Lowenthal et al. (1991) spectral energy distribution from the ultraviolet to the optical indicates

that the continuum flux would be $< 1.0x10^{-18}$ erg s^{-1} cm^{-2}Å^{-1}, below the 3σ detection limit $< 6.0x10^{-18}$ erg s^{-1} cm^{-2}Å^{-1} in the H band (neglecting dust extinction).

Figure 7 shows the sky-subtracted 2-D spectra for Lynx 2-9619. Labels mark the positions of the strong nebular lines. Figure 8 shows the infrared NIRSPEC N4, N6, N7 band spectra of Lynx 2-9691. Night sky emission lines appear below each target spectrum, scaled arbitrarily. An atmospheric transmissivity curve based on models for Mauna Kea (Lord 1992) is plotted above each spectrum, scaled arbitrarily, with a horizontal scale bar indicating zero transmissivity. Marks denote the expected redshifted positions of [O II] λ3727, Hβ, [O III] $\lambda\lambda$4959/5007, and Hα. In some cases, poor atmospheric transmissivity strongly affects the detectability of the line. Hα is lost amidst the night sky lines and strong atmospheric absorption longward of 2.5 μm. [O III] λ5007 is a strong detection, while [O III] λ4959 is not detected. A night sky line near the position of Hβ makes measurement of this line difficult, though emission is clearly seen on the 2-D image in Figure 7. The spike near [O II] λ3727 appears to be a residual cosmic ray, as no emission lines are present in the two-dimensional spectra. As with CFg, no continuum is present. Extrapolation from the UV continuum to the optical implies a flux level $< 1.0x10^{-18}$ erg s^{-1} cm^{-2}Å^{-1}, below the 3σ detection limit $< 7.0x10^{-18}$ erg s^{-1} cm^{-2}Å^{-1} in the N6 filter, well below the detection limit. Interestingly, [O III] λ5007 line is spatially extended over 20 pixels ($3.6''$=28 kpc) with a Gaussian FWHM of $2.0''$(16 kpc). This extended size is consistent on all three 900 s exposures. Images on the slit viewing camera show no signs of tracking problems, so we believe that this extension is real.

We measured the fluxes and velocity widths of emission lines using single 1-D Gaussian fits. Table 3 lists the values and upper limits, where appropriate. Since no continuum is detected in the infrared, the equivalent widths are undefined. From the $H\alpha$ fluxes, we compute the $H\alpha$ luminosities and star formation rates using the calibration of Kennicutt (1983). Table 3 summarizes these derived physical parameters for each system. For the CFg, the value of $F_{H\alpha} = 1.65 \pm 0.1 \times 10^{-16}$ erg s^{-1} cm^{-2} is in agreement with the narrowband imaging result of Bunker et al. (1995), who find $F_{H\alpha} = 2.1 \pm 0.6 \times 10^{-16}$ erg s^{-1} cm^{-2}. For our adopted cosmology, the star formation rates are 59 $M_\odot$ yr^{-1} and 111 $M_\odot$ yr^{-1} for the CFg and Lynx 2-9691, respectively. These values are 3-4 times higher than the mean value of 16 $M_\odot$ yr^{-1} for similarly luminous Lyman-drop galaxies (Steidel 1996b), but consistent with the 20-270 $M_\odot$ yr^{-1} found by Pettini et al. (1998) from Balmer recombination lines. In Table 3 we list the 1500 Å specific fluxes and luminosities, and the inferred SFR from the prescription of Madau, Pozzetti, & Dickinson (1998),

$$L_{1500} = 1.06 \times 10^{40} \times \frac{SFR}{(M_\odot\ yr^{-1})} erg\ s^{-1}\ \text{Å}^{-1}. \quad (2)$$

The SFRs derived from the Balmer lines in the CFg and Lynx 2-9691 are factors of $\sim 2-3$ times higher than those derived from the ultraviolet continuum specific luminosity at 1500 Å, 31 $M_\odot$ yr^{-1} for the CFg and 41 $M_\odot$ yr^{-1} for Lynx 2-9691. These differences may either imply significant amounts of dust extinction, or a systematic problem relating ultraviolet continuum fluxes to instantaneous star formation rates (see Glazebrook et al. 1998).

We calculate the intrinsic velocity width of the strongest emission line after the instrumental profile, defined by the width of night sky lines, has been subtracted in quadrature. This procedure makes the simplifying assumption that, due to seeing and target structure, the galaxy emission line is distributed uniformly across the width of the slit. For the CFg, the Hα line shows a FWHM of 301 km s^{-1}. The FWHM of [O III] is in good agreement at 250 km s^{-1}. Lynx 2-9691 has FWHM=156 km s^{-1} measured from the [O III] λ5007 line. Using the calculated velocity width, we estimate a *lower limit* for the virial mass of each system. As a fiducial dynamical size, we adopt the half-light radius (CFg) or the extent of the emission line gas (Lynx 2-9691). To estimate virial masses, we use the velocity full width at 20% of peak, $W_{20} = 3.62\sigma$ and half-light radius, r_{hl}, from Table 1 assuming $M_{vir} = \frac{(0.5W_{20})^2\ r_{hl}}{G}$ (e.g., Longair 1998), where G is the gravitational constant. The derived dynamical masses are $M_{vir} \geq 7.0 \times 10^{10}\ M_{\odot}$ for the CFg and $M_{vir} \geq 5.2 \times 10^{10}\ M_{\odot}$ for L2-9691. We stress that these dynamical masses are highly uncertain, in part because we lack information on inclination which make these values lower limits. Moreover, the dynamical size scale is difficult to constrain, the dynamical state of the system may not be in equilibrium, and the kinematic structure of the objects remains unknown.

4. Chemical Analysis

We have calculated an oxygen abundance for each object using the measured emission line strengths. Kobulnicky, Kennicutt, & Pizagno (1999) showed that whole-galaxy emission line ratios can provide a reliable indication of the system's nebular oxygen abundance using the empirical line flux ratio technique of Pagel et al. (1979).

$$R_{23} \equiv \left(\frac{[O\ II]\lambda 3727 + [O\ III]\lambda\lambda 4959, 5007}{H\beta} \right). \tag{3}$$

Several authors have published calibrations relating R_{23} to the oxygen abundance, O/H, including McGaugh (1991), Zaritsky, Kennicutt, & Huchra, (1994), McCall, Rybski, & Shields (1985), Edmunds & Pagel (1984), and Dopita & Evans (1986). Here, we adopt the McGaugh (1991) calibration, which is similar to the others over most metallicity regimes (see comparison Figure in Kobulnicky et al. 1999), and it has an analytic approximation making abundance computation more straightforward. From the line fluxes listed in Table 3, we have computed R_{23} along with the ionization parameter indicator O_{32}:

$$\log(O_{32}) \equiv \log\left(\frac{[O\ III]\lambda\lambda 4959, 5007}{[O\ II]\lambda 3727} \right). \tag{4}$$

Table 4 lists these line diagnostics for each object. In addition to the two objects observed here, we include 5 other infrared spectroscopic results at $z > 2$ from the literature (Teplitz et al. 2000a,b;

Pettini et al. 1998). Where [O II] λ3727 is not detected, we adopt $F_{3727} = 0.0$ and list a lower limit for R_{23}. When [O III] λ4959 is not detected, we assume the theoretical ratio $F_{4959} = F_{5007}/2.9$. For the CFg, where Hα is detected but $H\beta$ is not, we adopt $I_{H\beta} = I_{H\alpha}/2.86$ assuming theoretical case B hydrogen recombination ratios for gas with an electron temperature of 10,000 K (Hummer & Story 1987). This approximation is very insensitive to the actual electron temperature, but ignores effects of dust extinction. Any extinction correction would serve to raise R_{23} by boosting the strength of [O II] λ3727 relative to Hβ. We have also neglected the effects of stellar absorption on the Hβ line. Since no continuum is detected, we cannot even apply a statistical correction of 2–4 Å in the equivalent width, which is representative of local spiral galaxies (Kennicutt 1992). Thus, without many of the traditional constraints, any metallicity determination carries a significant uncertainty. We proceed to evaluate the results, while advocating a prudent amount of caution.

Figure 9 shows the diagnostic diagram R_{23} versus oxygen abundance, 12+log(O/H). The solid lines are models from McGaugh (1991) for realistic ranges of ionization parameter represented by $\log(O_{32})$. Each object from Table 4 is plotted either as an R_{23} lower limit, or a shaded box representing the probable location. The CFg is plotted as a lower limit with $\log R_{23} > 0.86$. For this object, we measure [O III] λ5007 and $H\alpha$. We infer $H\beta$ from Hα. There is no constraint on the extinction, and thus the actual $H\beta$ flux could be substantially less than the value adopted from the theoretical $H\alpha/H\beta$ ratio. The R_{23} lower limit constrains the oxygen abundance of the CFg to be $7.8 < 12 + log(O/H) < 8.7$. In computing the R_{23} lower limit, we have adopted $F_{3727} = 0$, while the measured upper limit is $F_{3727} < 0.47 \times 10^{-16}\ erg\ s^{-1}\ cm^{-2}$. For Lynx 2-9691, we have detected [O III] λ5007 at a high level of significance and Hβ at about the 3σ level. In computing the limits on R_{23}, we have constrained F_{3727} to lie between 0.0 and the 3σ upper limit of $F_{3727} < 0.50 \times 10^{-16}\ erg\ s^{-1}\ cm^{-2}$. H$\alpha$ lies in a region of high atmospheric opacity and is not detected. With these values, we constrain R_{23} to lie between $0.70 < R_{23} < 1.02$ while $\log(O_{32}) > 0.77$. Thus, we plot Lynx 2-9691 as a shaded strip in Figure 9, with an oxygen abundance in the range $8.3 < 12 + log(O/H) < 8.8$. For the moment, we have assumed that Lynx 2-9691 lies on the upper (metal-rich) branch of the empirical calibration. The other 4 targets in the literature, summarized in Table 4, have only lower limits on R_{23}, and thus we can only estimate their oxygen abundances within a broad range (see Figure 9). The best constrained is Q0201+113 C6 from Pettini et al. (1998) for which $7.7 < 12 + log(O/H) < 8.8$.

In principle, the metallicity of Lynx 2-9691 could also lie along conjugate position on the lower branch of the calibration, leading to $7.7 < 12 + log(O/H) < 8.0$. We argue that such extremely low metallicities are improbable for objects like Lynx 2-9691 and the luminous Lyman-drop galaxy population. The first piece of evidence is based upon the metallicity of MS1512-cB58, the first high-redshift object in the literature with a strong metallicity constraint (Teplitz et al. 2000a). As a highly-magnified Lyman-drop galaxy, all of the strong nebular emission lines are observed in MS1512-cB58, yielding $R_{23} = 0.92 \pm 0.07$ and $\log(O_{32}) = 0.17 \pm 0.04$. The probable range of the oxygen abundance becomes $8.2 < 12 + log(O/H) < 8.5$ consistent with the CFg and Lynx 2-9691. The nitrogen-to-oxygen ratio in MS1512-cB58 is $log(N/O) = -1.24$, indicating significant

levels of chemical enrichment by lower mass stars ($2M_{\odot} < M < 6M_{\odot}$; e.g. Pagel 1998; Lattanzio et al. 2000). In the local universe, and even in the intermediate-redshift universe at $z \sim 0.4$ (Kobulnicky & Zaritsky 1999), galaxies as metal poor as $7.7 < 12 + log(O/H) < 8.0$ also have low luminosities ($M_B > -18$). If lower branch metallicities were adopted for the $z \sim 3$ objects, then they would deviate even more strongly than they do from the local metallicity-linewidth and metallicity-luminosity relations, as discussed in the next sections.

5. Discussion of Results

5.1. Evolution of Kinematic Properties

Studying the evolution of fundamental galaxy scaling relations is one way of understanding how galaxies evolve from the early universe to the present. The evolution of the luminosity-linewidth relation (i.e., Tully-Fisher) at higher redshifts has been investigated by several authors (Forbes et al. 1995; Vogt et al. 1996, 1997) who find small offsets < 0.5 magnitude from the local TF relation out to z=1.0, while others find more dramatic changes of 1-2 magnitudes (Simard & Pritchet 1998; Rix et al. 1997; Mallen-Ornelas et al. 1999). In these studies, galaxies are more luminous for a given linewidth when compared to local samples. However, the bluest galaxies deviate most strongly from the TF relation, suggesting that the conclusions are sensitive to target selection effects (Bershady et al. 1998). With the kinematic linewidths we derive here, supplemented by the objects from Pettini et al. (1998) and Teplitz et al. (2000a) in Table 4, we can begin to assess the status of the luminosity-velocity correlations at $z > 2.3$ and compare them to local galaxies.

Bullock et al. (2000) parameterize possible forms of the evolution for the luminosity-velocity correlation as

$$M_B = -18.71 - 2.5log\left[(1+z^{\alpha})^{\beta/\alpha}\right] - 6.76(log2v_m - 2.5) + 5logh \quad (5)$$

Here, z is the redshift, h the Hubble constant in units $H_0/100$, and v_m the maximum circular velocity of the galaxy halo, which we take to be the velocity on the flat part of the rotation curve, as in Bullock et al. (2000) and Gonzalez et al. (2000). The parameters α and β control the behavior of the relation as a function of redshift. In Figure 10 we show the form of the luminosity-velocity relation for redshifts of $z = 0, 1, 2$, and 3 when $\alpha = 1$ and $\beta = 3$. We plot the data for a sample of local galaxies used in Kobulnicky & Zaritsky (1999; star symbols) and local luminous HII galaxies (Telles & Terlevich 1997; open squares). The data for the high-redshift galaxies in Table 4 appear as open circles with error bars. The local data are corrected for inclination, but the $z \sim 0.4$ and $z \sim 3$ samples are only upper limits since inclinations are not known. While not intended to be a rigorously-selected sample, these data serve to illustrate the locus occupied by local galaxies with chemical and dynamical measurements. In computing the maximum circular velocities we adopt the prescription of Tully & Fouqué (1985),

$$W_R^2 = W_{20}^2 + W_t^2 - 2W_{20}W_t[1 - e^{-(W_{20}/W_c)^2}] - 2W_t^2 e^{-(W_{20}/W_c)^2}. \quad (6)$$

Here, W_R is the rotation full amplitude which is $2\times V_{max}$. $W_t = 38$ km s^{-1} is the width due to turbulent motions and $W_c = 120$ km s^{-1} is the transition point between galaxies having Gaussian and those having double-horned HI profiles.

The analytic relations in Figure 10 ($\alpha = 1$ and $\beta = 3$) are qualitatively consistent with the data at redshifts beyond $z = 2.3$, in that the zero point of the relation shifts toward larger luminosities at higher redshift. This figure shows that the high-redshift galaxies lie 1-3 magnitudes more luminous for their velocity width than most normal local galaxies. We note that such deviations can be found among luminous HII galaxies locally (Telles & Terlevich 1997; open squares) or among compact galaxies at intermediate redshift (Fig. 3 of Koo et al. 1995). Although there is some uncertainty as to whether the integrated emission linewidths reflect the full dynamical width of the galaxy (e.g., Lehnert & Heckman 1996), a sample of local galaxies studied in both 21 cm neutral hydrogen and optical emission lines shows generally good agreement (Kobulnicky & Gebhardt 2000; Telles & Terlevich 1993). Taken at face value, these data indicate a significant evolution in the luminosity-metallicity relation at early epochs. However, it remains to be established whether the Lyman-drop galaxies observed to date are representative of the galaxy population at large. Due to the sensitivity constraints, only the brightest objects have been observed. Perhaps, like local HII galaxies, the luminous Lyman drop galaxies are more luminous than local galaxies of similar linewidth simply because they are undergoing particularly strong, concentrated bursts of star formation with amplitudes exceeding those in any local galaxies. With typical blue luminosities of $M_B = -22.5$, these objects are more luminous than any known star-forming (non-AGN) objects in the local universe, so a suitable low-redshift comparison sample is not available.

5.2. Evolution of Chemical Properties

One general result of this paper is that the probable oxygen abundance of normal, but very luminous, star-forming galaxies at redshifts near $z = 3$ is subsolar by 0.2-0.6 dex, where the most recent solar photospheric value is 12+log(O/H)=8.83 (Grevesse & Sauval 1998). However, caution must be exercised when relating the oxygen abundance derived from these empirical emission methods to the solar oxygen abundance which is determined by meteoritic and solar studies. The zero-point of the empirical emission line calibration is subject to an uncertainty of ~ 0.2 dex relative to the solar photospheric measurement. However, *relative* abundance measurements comparing the high-redshift sample to local galaxies using similar emission line techniques are still interesting and are more robust.

With these data, we can begin to study the evolution of another fundamental galaxy scaling relation, that between luminosity and metallicity (e.g., Lequeux et al. 1979; French 1980; Faber 1973; Brodie & Huchra 1991; Skillman, Kennicutt, & Hodge 1989; Zaritsky, Kennicutt, & Huchra

1994; Richer & McCall 1995). The high-redshift sample here is best compared to local galaxies where metallicities are measured using the same empirical nebular line method. Figure 11 shows the correlation between local irregular and spiral galaxy oxygen abundances (crosses) from the compilation of Kobulnicky & Zaritsky (1999) and the high-redshift sample from Table 4 (filled circles). Solid squares denote local H II galaxies from the sample of Telles & Terlevich (1997; magnitudes corrected to the adopted cosmology). We also plot in Figure 11 the $z \sim 0.4$ sample of star forming galaxies from Kobulnicky & Zaritsky (filled triangles). The $z \sim 0.4$ sample is statistically indistinguishable from the local galaxies. It is immediately obvious that the high-redshift sample is 2-4 magnitudes more luminous for their metallicity than either the local objects or the $z \sim 0.4$ sample. Objects at $z \sim 3$ deviate strongly from the local luminosity-metallicity relation in a manner similar to local H II galaxies. As noted by Kobulnicky & Zaritsky (1999), local H II galaxies from the sample of Telles & Terlevich (1997) appear ∼1-2 magnitudes more luminous for their metallicity for reasons not yet identified. It seems reasonable to propose that both the high-redshift sample and local H II galaxies are related in that they are both undergoing strong bursts of star formation which raise their luminosities above those of local galaxies with similar chemical composition and linewidth. It would be interesting to identify a local sample of star-forming galaxies for comparison to $z = 3$, but we are not aware of any local (non-AGN) sample which is suitably luminous.

Figure 11 illustrates qualitatively how the evolution of these high-redshift objects might proceed *if* they are the ancestors to local ellipticals and spiral bulges (Steidel et al.1996a,b; Lowenthal et al. 1997). Not only must they fade by 2-4 magnitudes, but they must also become more chemically rich by 0.2-0.5 dex in their gas phase oxygen abundance. (We note in the next section that the ISM metallicity in the high-z sample is consistent with the metallicity of bulge stars and metal-rich globular clusters in the Milky Way.) The solid arrow shows the direction of evolution if a combination of fading and continued metal enrichment are both dominant influences. The dashed arrow shows qualitatively the evolution if metal enrichment is suppressed by continued inflow of metal-poor gas as fading proceeds.

Figure 12 shows the correlation between oxygen abundance and kinematic velocity width, σ_v, for the same samples of objects plotted in Figure 11. Kinematic widths for local spiral and irregular galaxies, corrected for inclination, come from single-dish 21-cm measurements. Kinematic widths for the high and intermediate redshift sample, and for H II galaxies from Telles et al. (1997) are measured from Balmer lines with no inclination correction applied. All classes of objects are consistent with a well-defined relation between metallicity and kinematic width, except the $z \sim 0.4$ sample of star-forming galaxies from Kobulnicky & Zaritsky (1999). This intermediate redshift sample exhibits a smaller kinematic width than local galaxies of similar metallicity. However, since inclination corrections have not been applied, one plausible explanation is that these $z \sim 0.4$ objects are preferentially seen at low inclination. A larger sample of $z \sim 0.4$ objects with measured linewidths and oxygen abundances is needed to understand possible selection effects. Note that in this diagram, the dispersion in the metallicity-linewidth relation is much smaller than the dispersion

in the metallicity-luminosity plot of Figure 11. Presumably the tighter correlation is because both the oxygen abundance and linewidth are distance-independent and, to first order, extinction-independent quantities. Given the sophistication of today's galaxy evolution models, it would be worthwhile to compare the kinematic and chemical data in this figure with the popular semi-analytic simulations. At the present time, we are not aware of any suitable model velocity-metallicity tabulations in the literature. The models presented by Cole et al. (2000) show a dispersion of ~ 1 dex in metallicity for a given B-band luminosity (their Figure 10), suggesting that the dispersion in the model metallicities is larger than the dispersion observed in real galaxies.

5.3. Extended [O III] Emission in Lynx 2-9691

The spatially extended nature of the [O III] λ5007 line in Lynx 2-9691 is noteworthy in that we detect emission over a distance of $\sim$ 30 kpc. The line exhibits no detectable velocity shift ($<$120 km s^{-1}) along this extent. Not only does this extended morphology rule out a central AGN as the ionizing source, but it also means that hard photons capable of ionizing O^+ are distributed over a large region comparable to the size of the present day Milky Way. Although not as large as the $100h^{-1}$ kpc Lyman α nebulae discovered around Lyman drop galaxies (Steidel et al. 2000), the physical origin may be the same. Steidel et al. proposed that the Lyman α nebulae are produced either by star formation (which is heavily obscured along our line of sight so that the stellar continuum is not observed) or within cooling flows. However, the large velocity spread of 2000 km s^{-1} in the Steidel et al. objects is not observed here. Since the stellar continuum is not detected in the IR spectra of Lynx 2-9691, we cannot address the spatial distribution of the nebulae with respect to the galaxy, except to note that the direct image of the object appears starlike. Examination of 2-D LRIS spectra in which we detect the Lyman α line (Figure 1b) shows a stellar continuum size consistent with the seeing disk of 0.9″ FWHM. The Lyman α emission is only slightly more extended with a FWHM of 1.1″. The [O III] emission seen in the IR spectra is clearly much more extended than either the UV stellar continuum or the Lyman α emission. However, a direct comparison at the same position angle is not possible with the current data.

As mentioned previously, it is possible that Lynx 2-9691 is lensed by the $z = 0.31$ early type galaxy Lynx 2-9689. If so, the spatially-extended [O III] seen in the NIRSPEC slit might be part of the lensed arc while the LRIS slit which crosses perpendicular to the arc would yield only a small emission region. Simple lensing models show that the $z = 0.31$ galaxy needs to have a velocity dispersion of $\geq$ 300 km s^{-1} to serve as a lens that amplifies the $z = 2.9$ galaxy by several times along the arc and still be compatible with the 3.5″ separation.

5.4. The Descendants of Lyman Break Galaxies

Gas phase oxygen abundances of Lyman-drop galaxies can provide metallicity estimates for the underlying stellar population. The warm ionized component of the ISM in local starbursts is chemically homogeneous on scales of several kpc and shows no signs of localized chemical enrichment in the immediate vicinity of the starburst (Kobulnicky & Skillman 1996; 1997). Metals from massive starbursts may be entrained within the hot interior of wind-driven superbubbles and be vented into galactic halos before cooling and mixing with the neutral and molecular gas (Tenorio-Tagle 1996; MacLow & Ferrara 1999). Thus, it is reasonable to assume that *the recently-formed massive stars in Lyman-drop galaxies have metallicities very similar to that of the warm ISM, between 0.25* $Z_{\odot}$ *and 0.9* $Z_{\odot}$*.* Corroborating evidence comes from Pettini et al. (2000) who conclude that the stellar and interstellar absorption features in MS 1512-cB58 indicate a metallicity of $Z \sim 0.25 Z_{\odot}$ for the massive stars and intervening cool gas. Teplitz et al. find a similar metallicity ($Z \sim 0.3 Z_{\odot}$) from the oxygen abundance of the warm ionized gas (Teplitz et al. 2000b).

If the intense star formation activity seen in Lyman-drop galaxies represents the dominant star formation episodes for today's spiral bulges or giant ellipticals, then the evolved descendants in the local universe should exhibit similarly subsolar metallicities in their dominant stellar populations which formed 8-10 Gyr ago. However, if the Lyman-drop galaxies are the building blocks which undergo a series of mergers to form present-day bulges and ellipticals (Lowenthal et al. 1997), then any relationship between stellar age and metallicity would be substantially more complicated. In hierarchical galaxy formation scenarios (e.g., White & Rees 1978; Searle & Zinn 1978; Blumenthal et al. 1984; Kauffman et al. 1993; Cole et al. 1984; Somerville et al. 2000), galaxies grow by mergers of dark matter halos and accumulation of sub-galactic fragments. These types of models predict large dispersions in the age-metallicity relations. Such large variations are actually observed in Galactic halo stars and Galactic globular clusters (Carney 1996; Côté et al. 2000). The large dispersion observed in the age-metallicity relationship of Milky Way stars suggests a rather complex evolutionary scenario (Edvardsson et al. 1993; Friel & Janes 1993) for the Galactic disk as well.

It is interesting to compare the ISM metallicities of the $z \sim 3$ Lyman-drop objects in Table 4 ($Z = 0.25 - 0.95\ Z_{\odot}$) with the mean metallicities of damped Lyman α systems at similar redshifts. Pettini et al. (1997) and Lu et al. (1996) derive much lower metallicities, between 1/300 $Z_{\odot}$ and 1/10 $Z_{\odot}$, in absorption line systems at similar redshifts. The straightforward interpretation of this metallicity difference is that damped Lyman α measurements sample a different population of objects, or at least a very different physical volume, than the luminous Lyman-drop galaxies which harbor most of the star formation activity (see Pettini et al. 1998).

It is also interesting to compare the mean ISM metallicity of the objects in Table 4 ($Z \sim 0.3 Z_{\odot} \equiv [O/H] \sim -0.4 \pm 0.3$) to the mean metallicity of Galactic bulge stars and metal-rich Galactic globular clusters summarized in Côté et al. (2000): $[Fe/H] \sim -0.3$ for bulge stars and $[Fe/H] \sim -0.6$ for metal-rich Galactic globular cluster. Outside the Milky Way, in giant ellipticals, the metallicity of the metal-rich globular clusters is known to correlate with the mass of

the parent galaxy (Forbes, Brodie, & Grillmair 1997), varying between $-0.4 < [Fe/H] < 0.0$. Evidently the formation and evolution of these metal-rich globular clusters is coupled to that of the parent galaxy and they represent the galaxy's intrinsic cluster population (Côté et al. 1998). Assuming $[Fe/O]$ ∼0.0, as is typical for Galactic stars with $[Fe/H] > -1$ (Wheeler, Sneden & Truran 1989), we can compare the metallicities of the ISM in Lyman-drop galaxies to the stellar components in nearby galaxies. *The metallicity of the ISM in the Lyman-drop galaxies tabulated here,* $[O/H] \sim -0.4 \pm 0.3$*, is consistent with the metallicities needed to form the metal-rich globular cluster population in the Milky Way,* $[Fe/H] \sim -0.6 \pm 0.2$. Many of the Galaxy's bulge and disk stars have metallicities and ages that would be consistent with their formation in a galaxy like Lynx2-9691 at $z = 2.9$ as well.

6. Conclusions

The mean metallicities of $z \sim 3$ galaxies lie in the range $Z = 0.25 - 0.95\ Z_{\odot}$, considerably more metal-rich than the mean damped Lyman α systems observed at the same redshift which have $Z \leq 0.1\ Z_{\odot}$ (Pettini et al. 1997; Lu et al. 1996). Based on the limited data available to date, the population of star-forming galaxies at ~ 3 is found to be 2-4 magnitudes more luminous than galaxies of similar rotational velocity and metallicity today. If these galaxies are representative of the populations at early times, then the fundamental galaxy scaling relations, namely the luminosity-velocity and luminosity-metallicity relation may be significantly different at $z > 2.3$ compared to the present. If, however, we are only viewing the peak of the luminosity function, perhaps the result of being viewed during the earliest phases of a strong burst of star formation, then these data may merely indicate a larger dispersion of luminosities at high-redshift compared to today. The gas-phase metallicities of Lyman-drop galaxies studied here are comparable to the metallicities needed to form stars in Galactic metal-rich globular clusters and bulge. With the arrival of many 8-10 m class telescopes with near-IR spectrographs, we expect that these early, and still uncertain, results will soon be supplemented by large enough samples to begin statistical studies of the velocity and chemical properties at $z > 2.3$ at the same significance level as that of photometric and morphological studies at high-redshift.

7. Acknowledgments

We thank the NIRSPEC instrument team for bringing such a successful instrument to fruition, and the Keck staff for their support, especially Greg Wirth who assisted with observations at the telescope. Nicolas Cardiel cleverly solved a problematic flux calibration issue. Thanks to James Lowenthal for providing optical spectra of the Coup Fourré galaxy in electronic form and he and Nathan Roche for early access to their paper on the CFg. Matt Bershady provided the scanned plate image of Lynx 2-9691. We gratefully acknowledge educational exchanges with Matt Bershady, James Bullock, Dirk Fabian, Jay Gallagher, Max Pettini, Philipp Richter, Rachel Somerville, Chuck

Steidel, and Harry Teplitz. This work was supported by a faculty research grant from the University of California, Santa Cruz, and an NSF grant AST-9529098. H. A. K is grateful for support from Hubble Fellowship grant #HF-01094.01-97A awarded by the Space Telescope Science Institute which is operated by the Association of Universities for Research in Astronomy, Inc. for NASA under contract NAS 5-26555.

REFERENCES

Bershady, M. A., Haynes, M. P., Giovanelli, R., & Andersen, D. R. 1998, in Galaxy Dynamics, eds. D. R. Merritt, M. Valluri, & J. A. Sellwood (ASP Conf Series)

Blumenthal, G. R., Faber, S. M., Primack, J. R., & Rees, M. J. 1984, Nature, 311, 517

Bohlin, R. C. 1996, AJ, 111, 1743

Bohlin, R. C. 2000, AJ, in press

Brodie, J. P., & Huchra, J. P. 1991, ApJ, 379, 157

Bullock, J. S., Dekel, A., Primack, J. L., & Somerville, R. S. 2000, MNRAS, submitted

Bunker, A. J., Warren, S. J., Hewett, P. C., & Clements, D. L. 1995, MNRAS, 273, 513

Carney, B. W., Laird, J. B., Lathan, D. W., & Aguilar, L. A. 1996, AJ, 112, 668

Cen, R., & Ostriker, J. P. 1999, ApJ, 519, L109

Côté, P., Marzke, R. O., West, M. J. 1998, ApJ, 554, 570

Côté, P., Marzke, R. O., West, M. J., & Minniti, D. 2000, ApJ, 533, 869

Cole, S., Aragón-Salamanca, A., Frenk, C. S., Navarro, J. F., & Zepf, S. E. 1994, ApJ, 495, L1

Dickinson, M. 2000, Phil. Trans. of the Royal Society, A, in press

Dopita, M. A., & Evans, I. N. 1986, ApJ, 307, 431

Edmunds, M. G. & Pagel, B. E. J. 1984, MNRAS, 211, 507

Edvardsson, B., Andersen, J., Guftafsson B., et al. 1993, A&A, 275, 101

Faber, S. M. 1973, ApJ, 179, 423

Forbes, D. A., Brodie, J.P., & Grillmair, C. F. 1997, AJ, 113, 1652

Forbes, D. A., Phillips, A. C., Koo, D. C., & Illingworth, G. D. 1995, ApJ, 462, 89

French, H. B., 1980, ApJ, 240, 41

Friel, E. D. & Janes, K. A. 1993, A&A, 267, 75

Fukugita, M., Shimasaku, K., & Ichikawa, T. 1995, PASP, 107, 945

Glazebrook, K., Abraham, R., Santiago, B., Ellis, R., & Griffiths, R. 1998, MNRAS, 297, 885

Gonzalez, A. H., Williams, K. A., Bullock, J. S., Kolatt, T. S., & Primack, J. R. 2000, ApJ, 528, 145

Grevesse, N. & Sauval, A. J. 1998, Space Science Reviews, 85, 161

Hummer, D. G., & Storey, P. J. 1987, MNRAS, 224, 801

Kauffman, G., White, S. D. M., & Guiderdoni, B. 1993, MNRAS, 264, 201

Kennicutt, R. C. Jr. 1983, ApJ, 272, 54

Kennicutt, R. C. Jr. 1992, ApJS, 79, 255 (K92)

Kobulnicky, H. A., Kennicutt, R. C., & Pizagno, J. L. 1999, ApJ, 514, 544

Kobulnicky, H. A. & Gebhardt, K. 2000, AJ, 119, 1608

Kobulnicky, H. A., & Skillman, E. D. 1996, ApJ, 471, 211

Kobulnicky, H. A., & Skillman, E. D. 1997, ApJ, 489, 636

Kobulnicky, H. A., & Zaritsky, D. 1999, ApJ, 511, 188

Koo, D. C., Guzman, R., Faber, S. M., Illingworth, G. D. Bershady, M. A., Kron, R. G., & Takamiya, M. 1995, ApJ, 440, L49

Kron, R. G. 1980, ApJS, 43, 305

Lattanzio, J. C., & Pettini, M., Tout, C. A., & Carigi, L. 2000, A&A, in press

Lehnert, M. D., & Heckman, T. M. 1996, ApJ, 472, 546

Lequeux, J., Peimbert, M., Rayo, J. F., Serrano, A., & Torres–Peimbert, S. 1979, A&A, 80, 155

Longair, M. S. 1998, Galaxy Formation (Springer:New York)

Lord, S.D. 1992, NASA Technical Memor. 103957

Lowenthal, J. D., Hogan, C. J., Green, R. F. Caulet, A., Woodgate, B. E., Brown, L., & Foltz, C. B. 1991, ApJ, 377, L73

Phillips, A. C., Guzman, R., Gallego, J., Koo, D. C., Lowenthal, J. D., Vogt, N. P., Faber, S. M., & Illingworth, G. D. 1997, ApJ, 489, 543

Lu, L., Sargent, W. L. W., Barlow, T. .A., Churchill, C. W., & Vogt, S. 1996, ApJS, 107, 475

MacLow, M. M, & Ferrara, A. 1999, ApJ, 513, 142

Madau, P. Ferguson, H. C., Dickinson, M. E., Giavalisco, M., Steidel, C. C., & Fruchter, A. 1996, MNRAS, 283, 1388

Madau, P., Pozzetti, L., & Dickinson, M. 1998, ApJ, 498, 106

Mallen-Ornelas, G., Lilly, S. J., Crampton, D. S. 1999, ApJ, 518, L83

McCall, M. L., Rybski, P. M., & Shields, G. A. 1985, ApJS, 57, 1 (MRS)

McGaugh, S. 1991, ApJ, 380, 140

McLean, I. S., et al. 2000, PASP, preprint

Munn, J. A., Koo, D. C., Kron, R. G., Majewski, S. R., Bershady, M A., Smetanka, J. J. 1997, ApJS, 109, 45

Neubig, M. M., & Bruhweiler, F. C. 1999, AJ, 117, 2856

Oke, J. B. 1990, AJ, 99, 1621

Oke, J. B., et al. 1995, PASP, 107, 375

Pagel, B. E. J., Edmunds, M. G., Blackwell, D. E., Chun, M. S., & Smith, G. 1979, MNRAS, 189, 95

Pagel, B. E. J. 1998, "Nucleosynthesis and Chemical Evolution in Galaxies", (Cambridge Press; New York)

Pei, Y. C., Fall, S. M., & Hauser, M. G. 1999, AJ, 522, 604

Pettini, M., Kellog, M., Steidel, C. C., Dickinson, M., & Giavalisco, M. 1998, ApJ, 508, 539

Pettini, M., Steidel, C. C., Adelberger, K. L., Dickinson, M., & Giavalisco, M. 2000, ApJ, 528, 96

Pettini, M., Smith, . J., King, D. L., Hunstead, R. W. 1997, APJ, 486, 665

Pickels, A. J. 1988, PASP, 110, 863

Prochaska, J. X. & Wolf, A. M. 1999, ApJS, 121,369

Prochaska, J. X. & Wolf, A. M. 2000, ApJ, 533, L5

Richer, M. G., & McCall, M. L. 1995, ApJ, 445, 642

Rix, H. W., Guhathakurta, P., Colless, M., & Ing, K. 1997, MNRAS, 285, 779

Roche, N., Lowenthal, J. D., & Woodgate, B. 2000, MNRAS, in press

Schulte-Ladabeck, R. E., Hillier, D. J., & Herald, J. E. 1995, ApJ, 4564, L51

Searle, L., & Zinn, R. 1978, ApJ, 225, 357

Seitz, S., Saglia, R. P., Bender, R., Hopp, U., Belloni, P., & Ziegler, B. 1998, MNRAS, 298, 945

Simard, L., & Pritchet, C. J. 1998, ApJ, 505, 96

Skillman, E. D., Kennicutt, R. C., & Hodge, P. 1989, ApJ, 347, 875

Sommerville, R. R., Primack, J. R., & Faber, S. M. 2000, MNRAS, in press

Steidel, C. C. 1999, Proc. Nat. Ac. Sci., 96, 4232

Steidel, C. C., Giavalisco, M., Pettini, M., Dickinson, M., & Adelberger, K. L. 1996a, ApJ, 462, L17

Steidel, C. C., Giavalisco, M., Dickinson, M., & Adelberger, K. L. 1996b, AJ, 112, 352

Steidel, C. C., Adelberger, K. L., Giavalisco, M., Dickinson, M. & Pettini, M. 1999, ApJ, 519, 1

Steidel, C. C., Adelberger, K. L., Shapley, A. E., Pettini, M., Dickinson, M., Giavalisco, M. 2000, ApJ, 532, 170

Stern, D., & Spinrad, H. 1999, PASP, 111, 1475

Telles, E. & Terlevich, R. 1993, Ap&SS, 205, 49

Telles, E. & Terlevich, R. 1997, MNRAS, 286, 183

Tenorio-Tagle, G. 1996, AJ, 111, 1641

Teplitz, H. I., Malkan, M. A., Steidel, C. C., McLean, I. S., Becklin, E. E., Figer, D. F., Gilbert, A. M., Graham, J. R., Larkin, J. E., Levenson, N. A., & Wilcox, M. K. 2000a, ApJ, in press

Teplitz, H. I., McLean, I. S., Becklin, E. E., Figer, D. F., Gilbert, A. M., Graham, J. R., Larkin, J. E., Levenson, N. A., & Wilcox, M. K. 2000b, ApJ, 533, L65

Thejll, P., Ulla, A., & MacDonald, J. 1995, A&A, 303, 773

Tully, R. B., & Fouqué, P. 1985, ApJS, 58, 67

Vogt, N., Forbes, D., Phillips, A. C., Gronwall, C., Faber, S. M., Illingworth, G. D., & Koo, D. C. 1996, ApJ, 465, L15

Vogt, N., Phillips, A. C., Faber, S. M., Gallego, J., Gronwall, C., Guzman, R., Illingworth, G., Koo, D. C., & Lowenthal, J. D. 1997, 479, L121

Wheeler, J. C., Sneden, C., & Truran, J. W. 1989, ARA&A, 27, 279

White, S. D. M., & Rees, M. J. 1978, MNRAS, 183, 341

Zaritsky, D., Kennicutt, R. C., & Huchra, J. P. 1994, ApJ, 420, 87

This preprint was prepared with the AAS LaTeX macros v5.0.

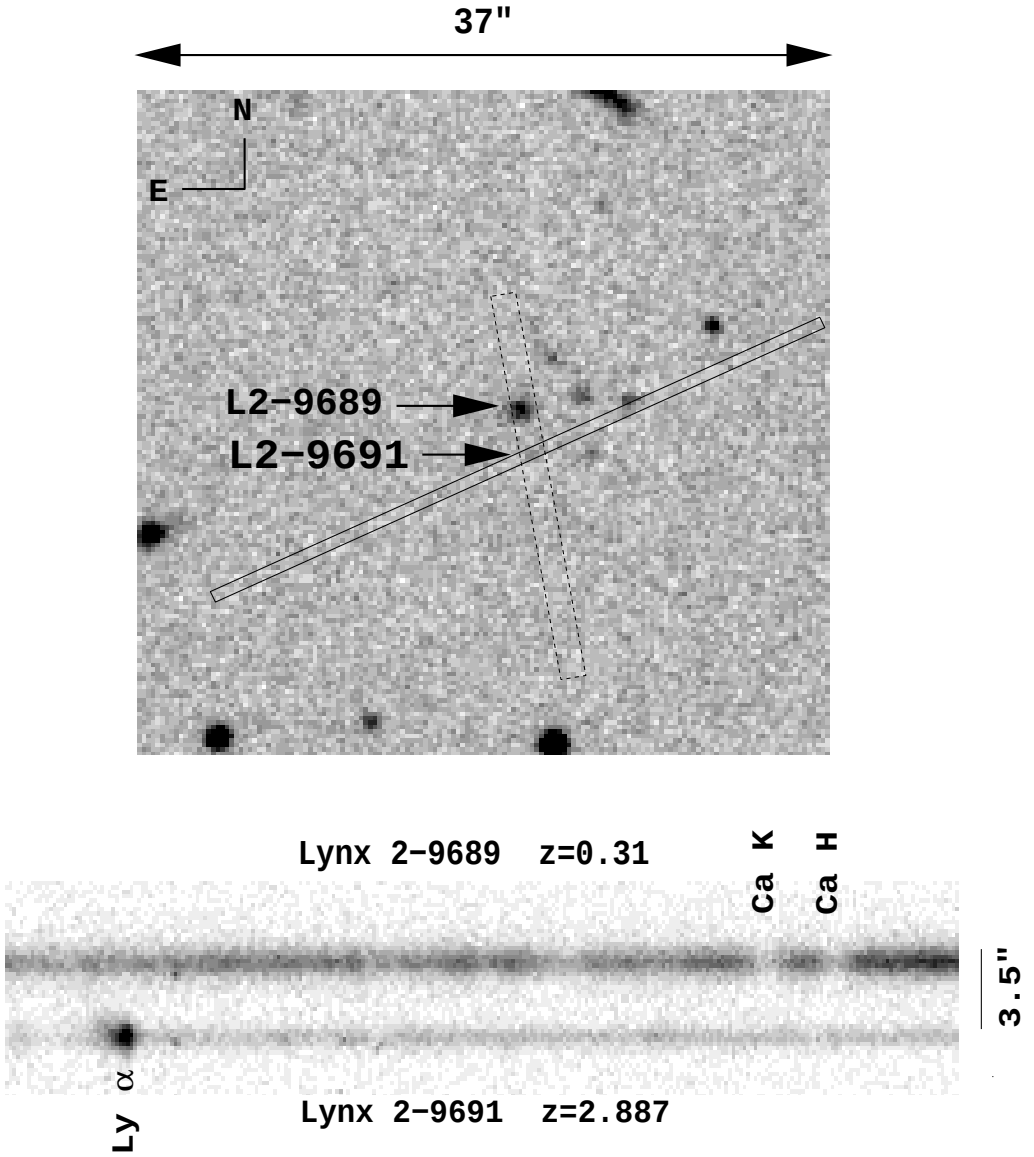

Fig. 1.— (a) Finding chart for Lynx 2-9691 from microdensitometer scans of a relatively deep 4-m prime focus photographic plate taken with the R_F filter (M. Bershady, private communication). Table 1 lists 2000 epoch coordinates. A solid rectangle marks the position of the NIRSPEC slit. A dashed rectangle denotes the position of the optical Keck/LRIS slitlet. (b)—Keck/LRIS discovery spectrum of Lynx 2-9691 showing Lyman α emission at $z = 2.8877$. An early-type galaxy, Lynx 2-9689, showing prominent Ca H&K $\lambda\lambda 3970, 3932$ absorption at $z = 0.31$, is located $3.5''$ to the northeast at a position angle of 10 degrees. The spatial scale of the CCD is $0.21''$/pix.

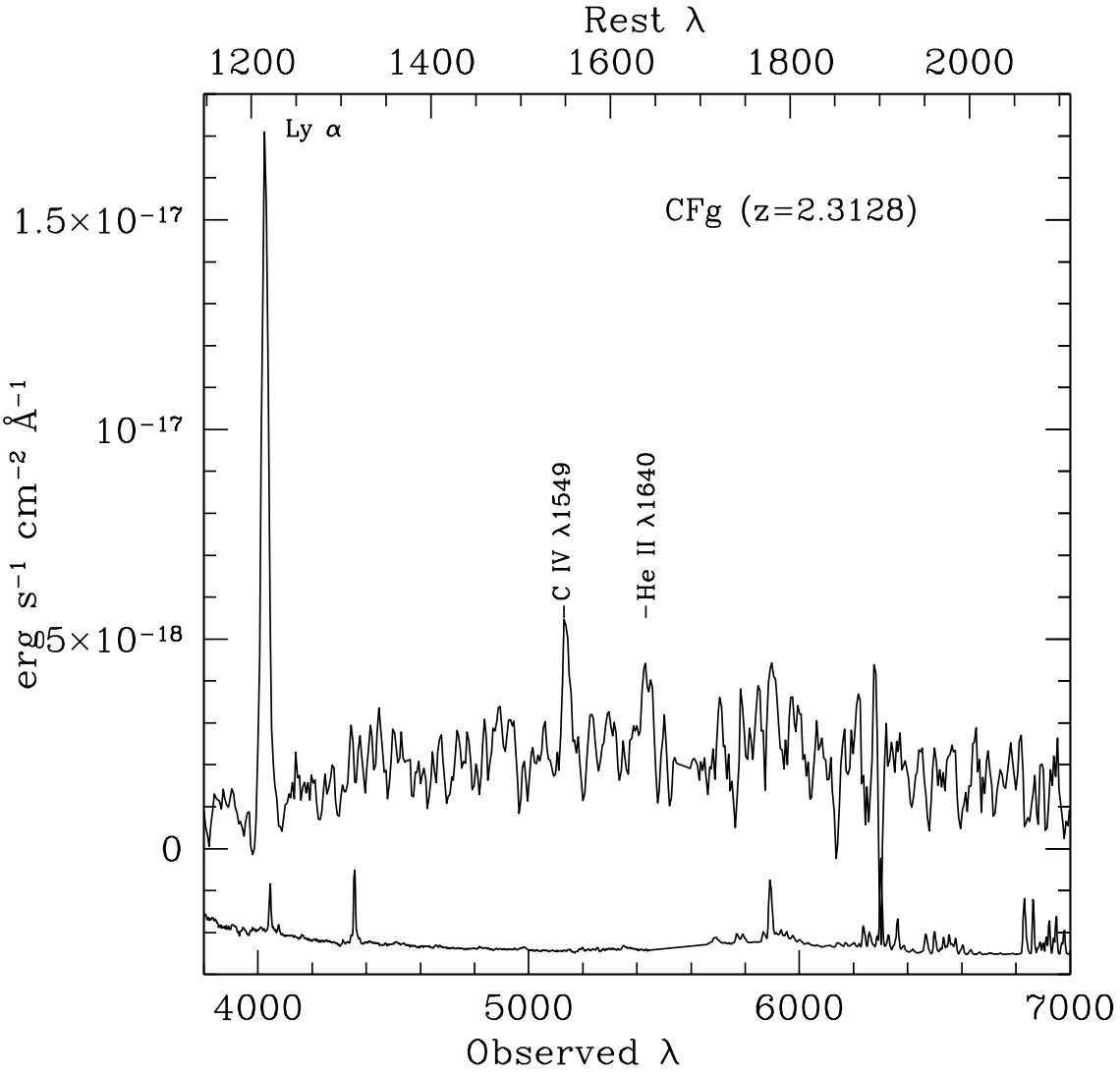

Fig. 2.— Optical spectrum of the Coup Fourré Galaxy (CFg) from Lowenthal et al. (1991). Lyman α and narrow emission lines from C IV λ1548/51 and He II λ1640 are visible. A representative night sky airglow spectrum is shown below, scaled arbitrarily. As in Lowenthal et al. (1991), the spectrum has been smoothed to a resolution of FWHM$\simeq$24 Å.

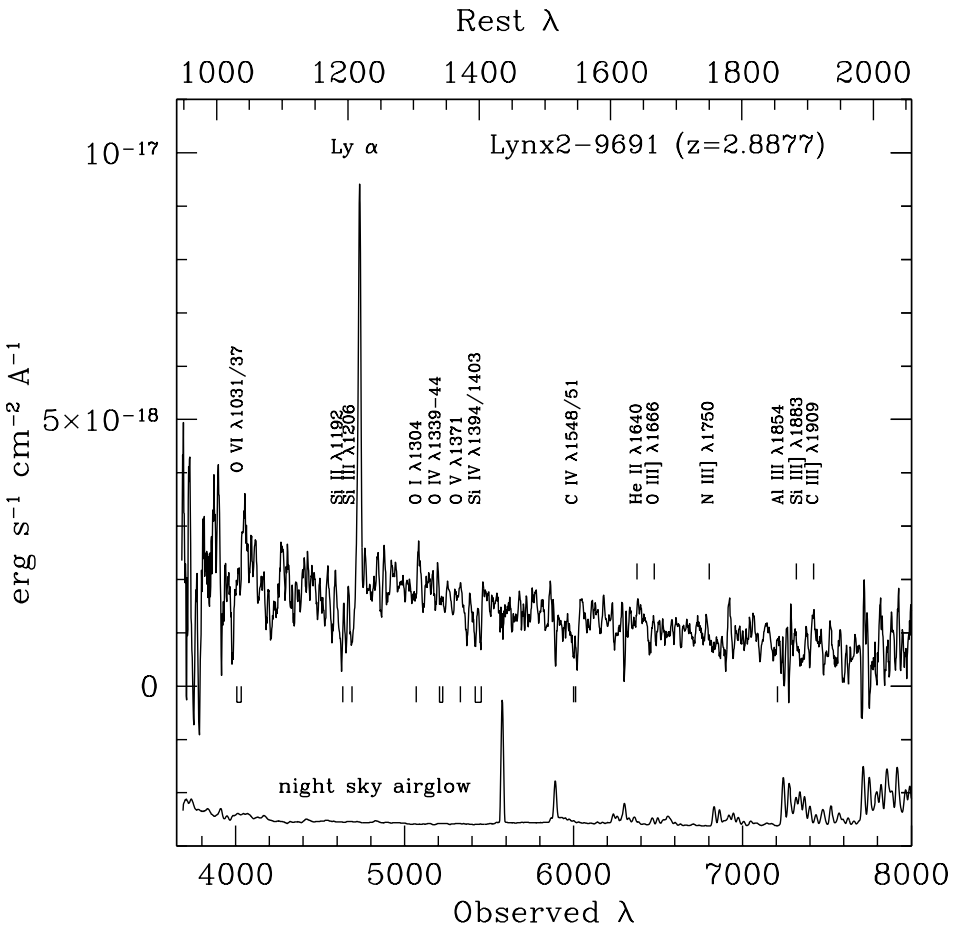

Fig. 3.— Keck LRIS optical spectrum of Lynx 2-9691 with a resolution of 9 Å FWHM. The spectrum has been smoothed with a 5-pixel boxcar for display purposes. A representative night sky airglow spectrum is shown below, scaled arbitrarily. Common interstellar emission and absorption lines allow us to derive a redshift of z=2.889 consistent with the z=2.8877 derived from the infrared spectra in Figure 6. The lack of broad lines and the preponderance of stellar absorption features, (see also Figure 4) is consistent with a normal star-forming galaxy rather than an active nucleus. As commonly seen in other Lyman-drop galaxies (Steidel et al.1996a,b; Pettini et al. 2000), the Lyman α centroid is shifted redward by 5 Å relative to the nominal position expected for its redshift, suggesting absorption of the blue wing by the galaxy's intervening ISM.

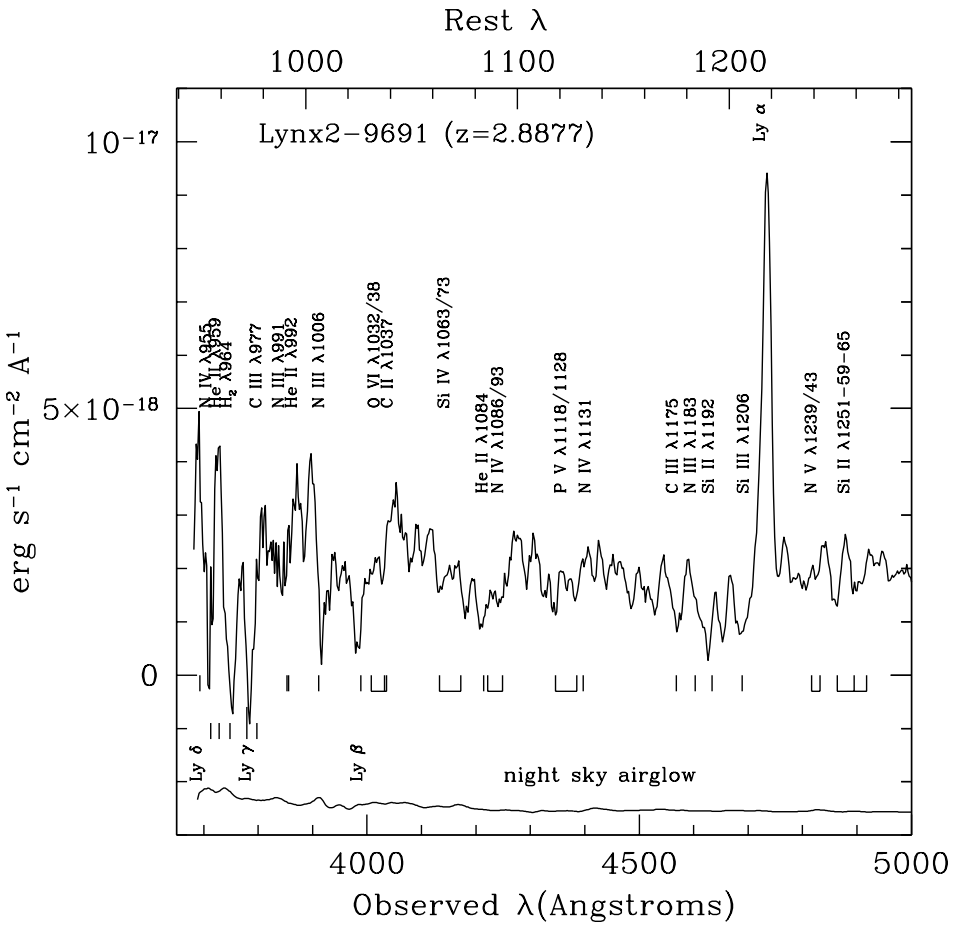

Fig. 4.— Enlargement of the far-ultraviolet portion of the Lynx 2-9691 spectrum. Strong stellar and interstellar absorption features dominate the spectrum. A representative night sky airglow spectrum is shown below, scaled arbitrarily.

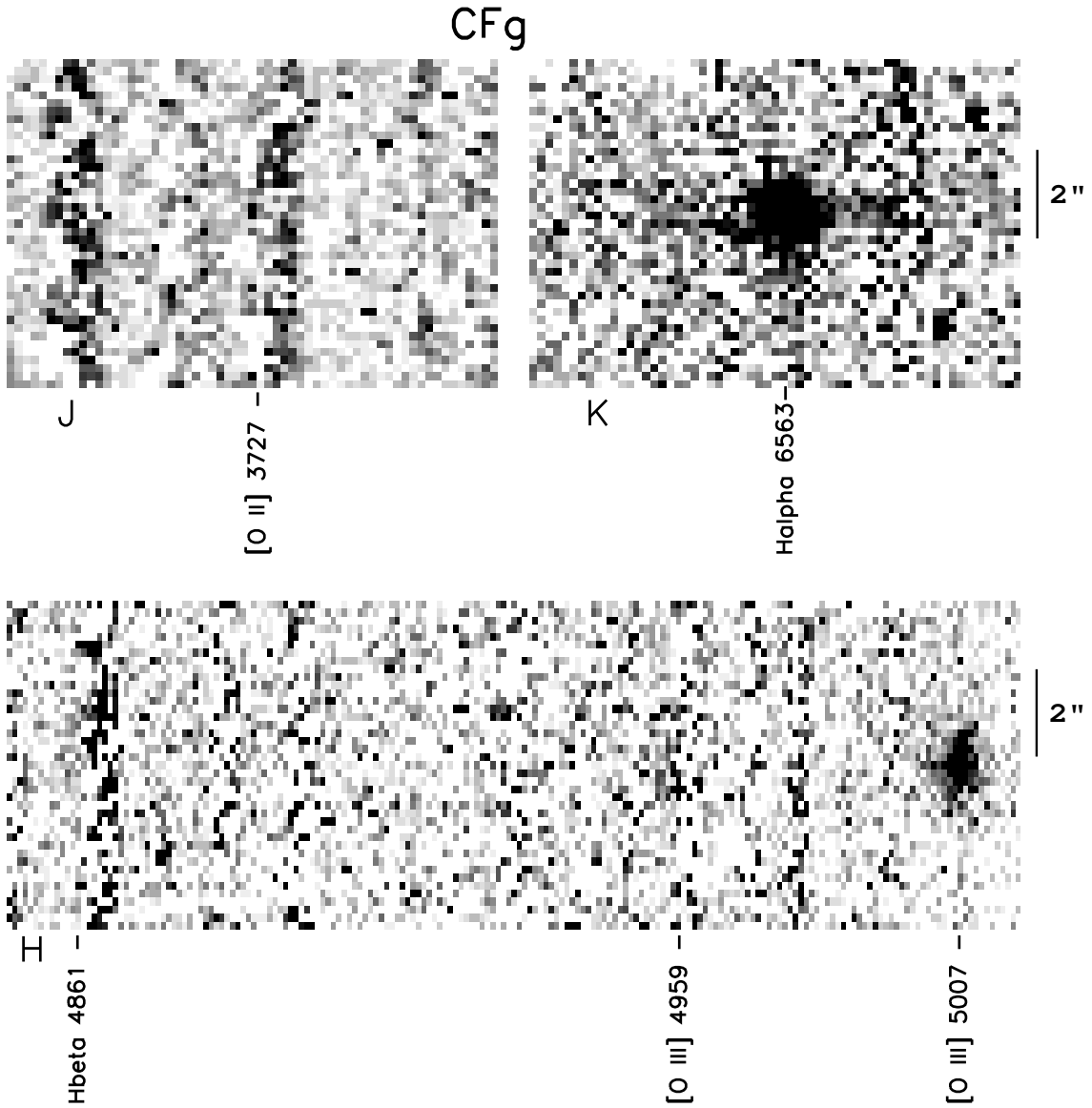

Fig. 5.— Two-dimensional sub-images of the Keck NIRSPEC spectra of the CFg in the J, H, and K infrared bandpasses. Positions of strong nebular emission lines are labeled. The scale is $0.178''$/pix in the spatial direction and ~ 3 Å/pix in the spectral direction. Labels mark the expected positions of strong nebular lines assuming $z = 2.3128$.

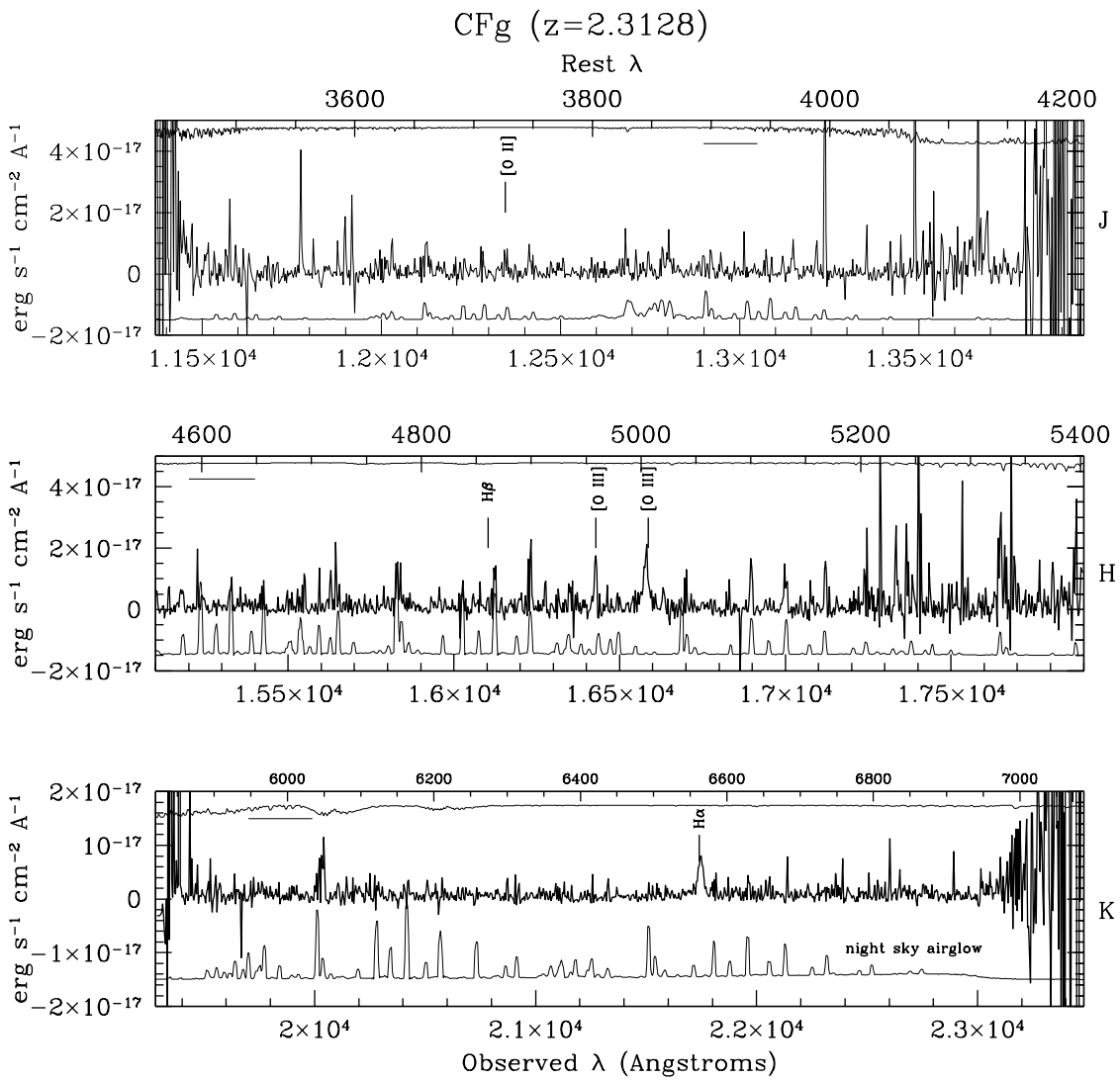

Fig. 6.— Keck NIRSPEC infrared spectra of the CFg in the J,H,K bandpasses. The positions of strong nebular emission lines are marked assuming $z = 2.3128$. For reference, a spectrum of the night sky airglow is plotted below, scaled arbitrarily. The atmospheric transmissivity curve based on models for Mauna Kea (Lord 1992) is plotted above each spectrum, scaled arbitrarily, with a horizontal scale bar indicating zero transmissivity.

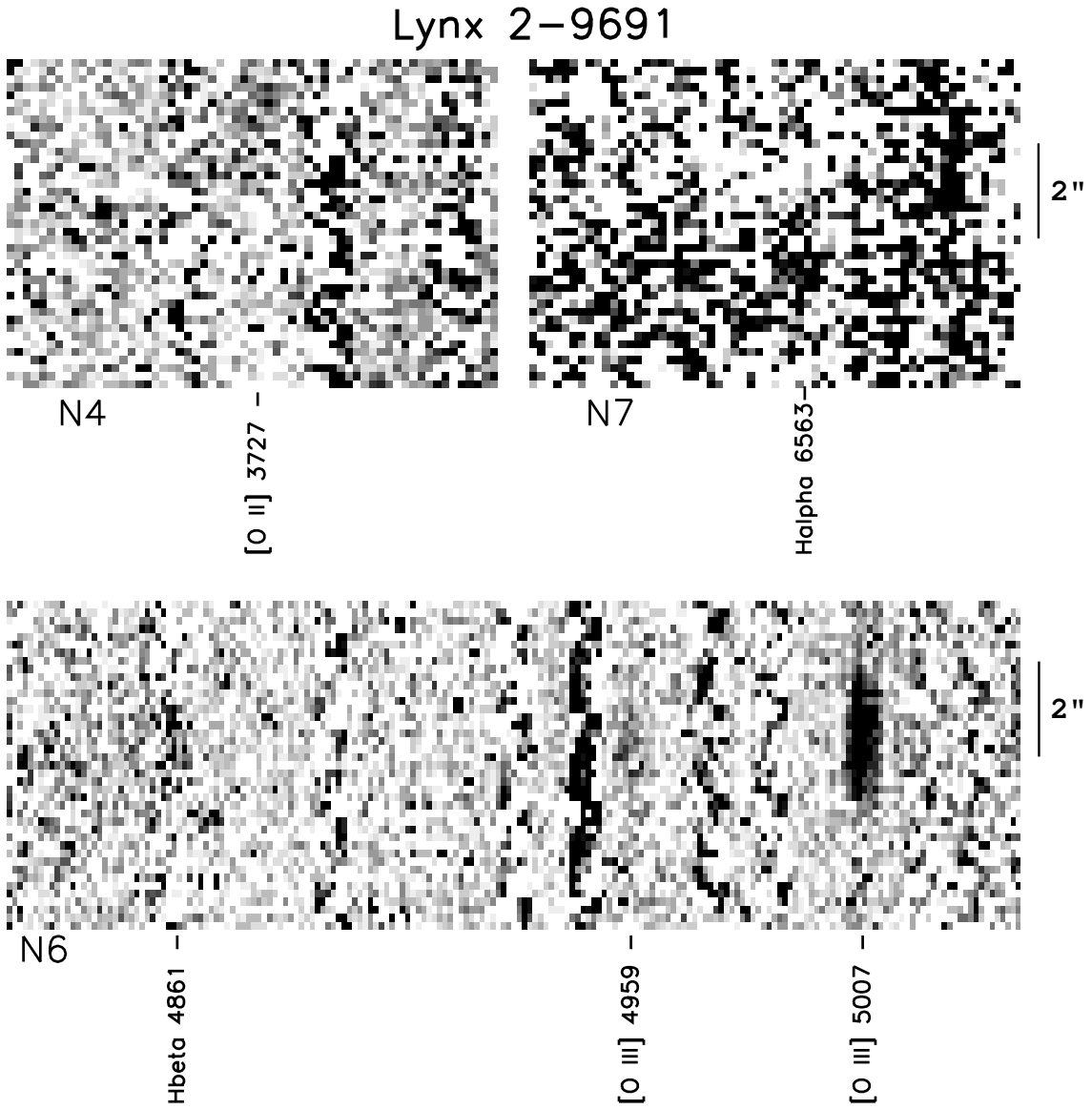

Fig. 7.— Two-dimensional sub-images of the Keck NIRSPEC spectra of Lynx 2-9691 in the NIRSPEC N4, N6, N7 infrared bandpasses. Positions of strong nebular emission lines are labeled assuming $z = 2.8877$. The scale is $0.178''$/pix in the spatial direction and ~ 3.8 Å/pix in the spectral direction. Labels mark the expected positions of strong nebular lines.

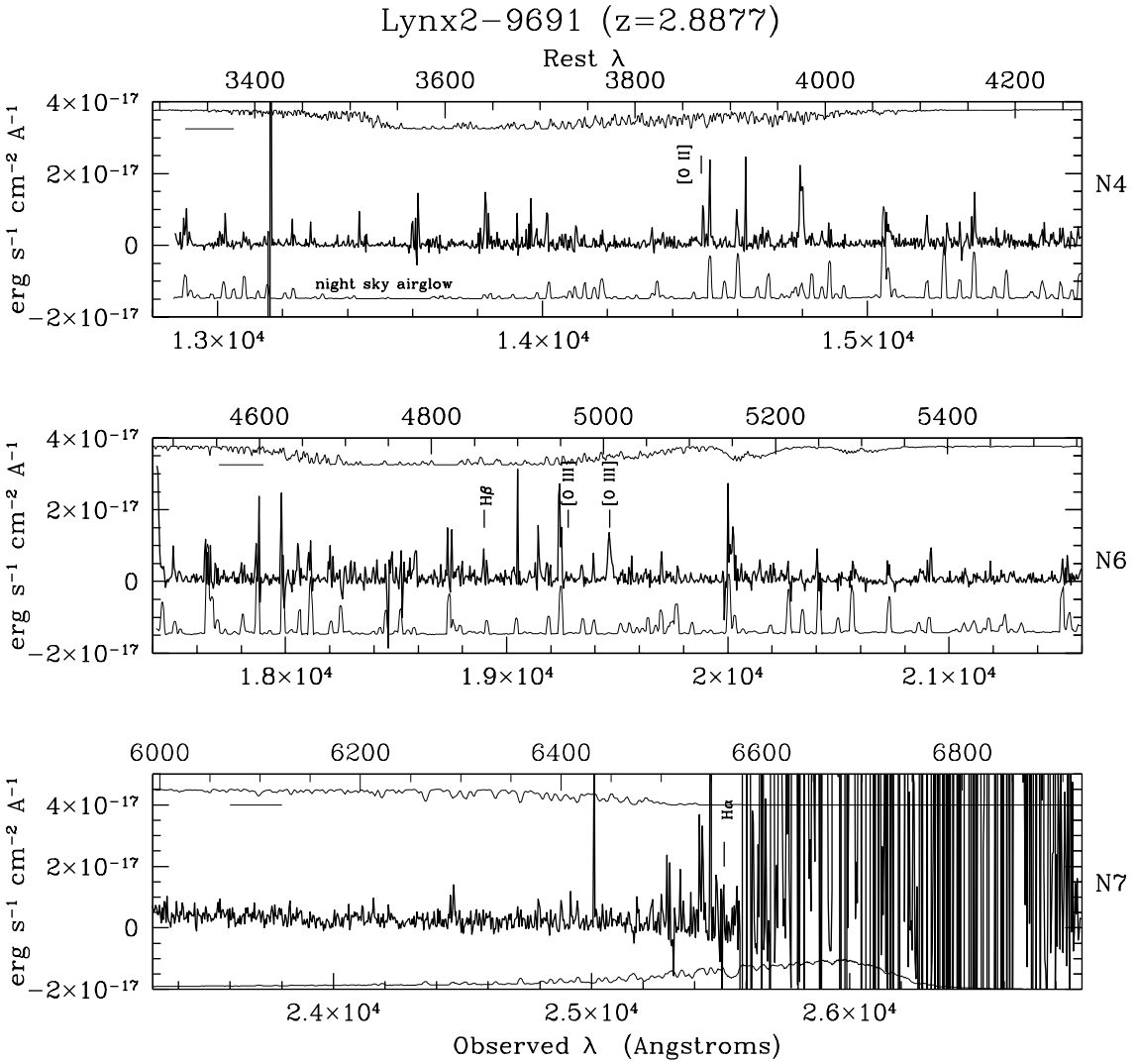

Fig. 8.— NIRSPEC infrared spectra of the CFg in the NIRSPEC N4,N6,N7 bandpasses. The positions of strong nebular emission lines are marked assuming $z = 2.8877$. For reference, a spectrum of the night sky airglow is plotted below, scaled arbitrarily. The atmospheric transmissivity curve based on models for Mauna Kea (Lord 1992) is plotted above each spectrum, scaled arbitrarily, with a horizontal scale bar indicating zero transmissivity. The spectrum becomes noisy beyond 2.5 μm because of thermal background emission.

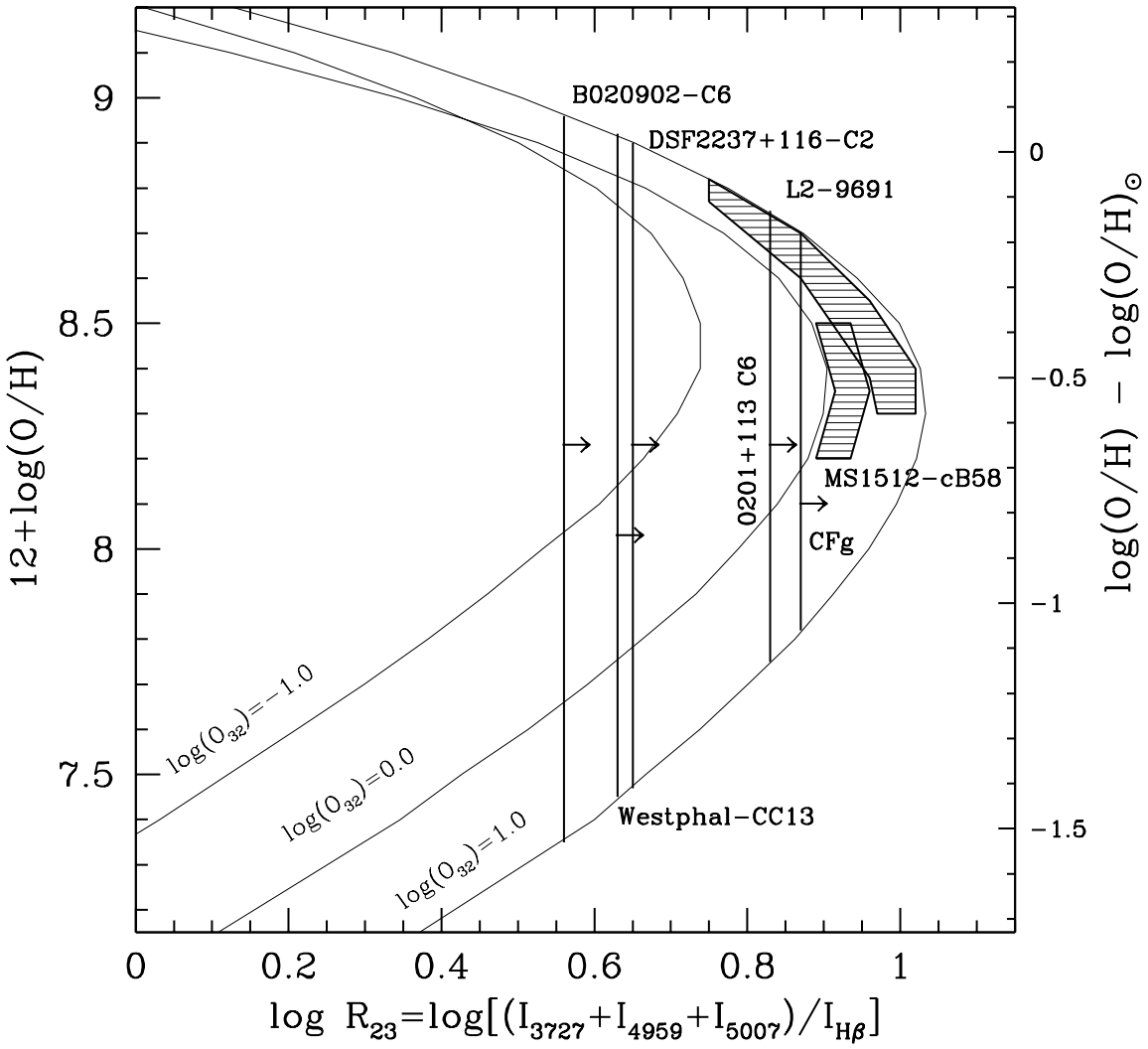

Fig. 9.— The diagnostic line ratio $R_{23} = [(I_{3727} + I_{4959} + I_{5007})/I_{H\beta}$ for high-redshift objects from the literature, and the corresponding oxygen abundance, 12+log(O/H), from the models of McGaugh (1991). Shaded boxes represent the most probable locations for the best-measured objects, Lynx 2-9691 and MS1512-cB58 (Teplitz et al. 2000b). Other objects with R_{23} lower limits are plotted spanning a range of possible metallicities.

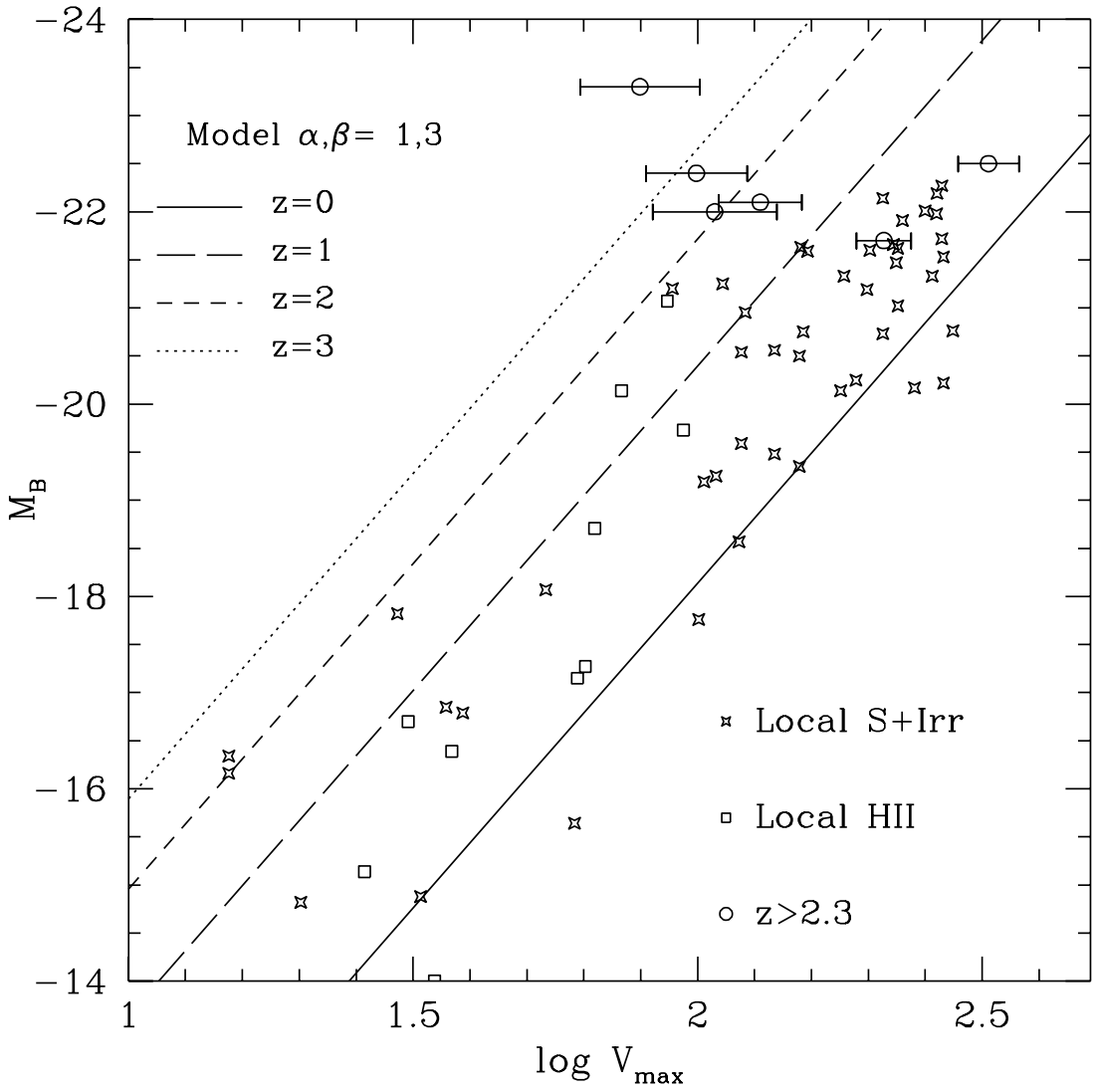

Fig. 10.— Evolution of the relation between luminosity, M_B, and circular velocity, v_m, as a function of redshift. The figure illustrates a range of possible evolution of the luminosity-velocity relation as a function of the α,β parameters of Bullock et al. (2000; see Equation 5). We show data for local spiral and irregular galaxies compiled in Kobulnicky & Zaritsky (1999). High-redshift objects from Table 4 appear as open circles with error bars, while local HII galaxies from Telles & Terlevich (1997) appear as open squares. Like local HII galaxies, $z \sim 3$ Lyman-drop galaxies are systematically more luminous for their velocity widths than spiral and irregular galaxies in the local luminosity-linewidth correlation.

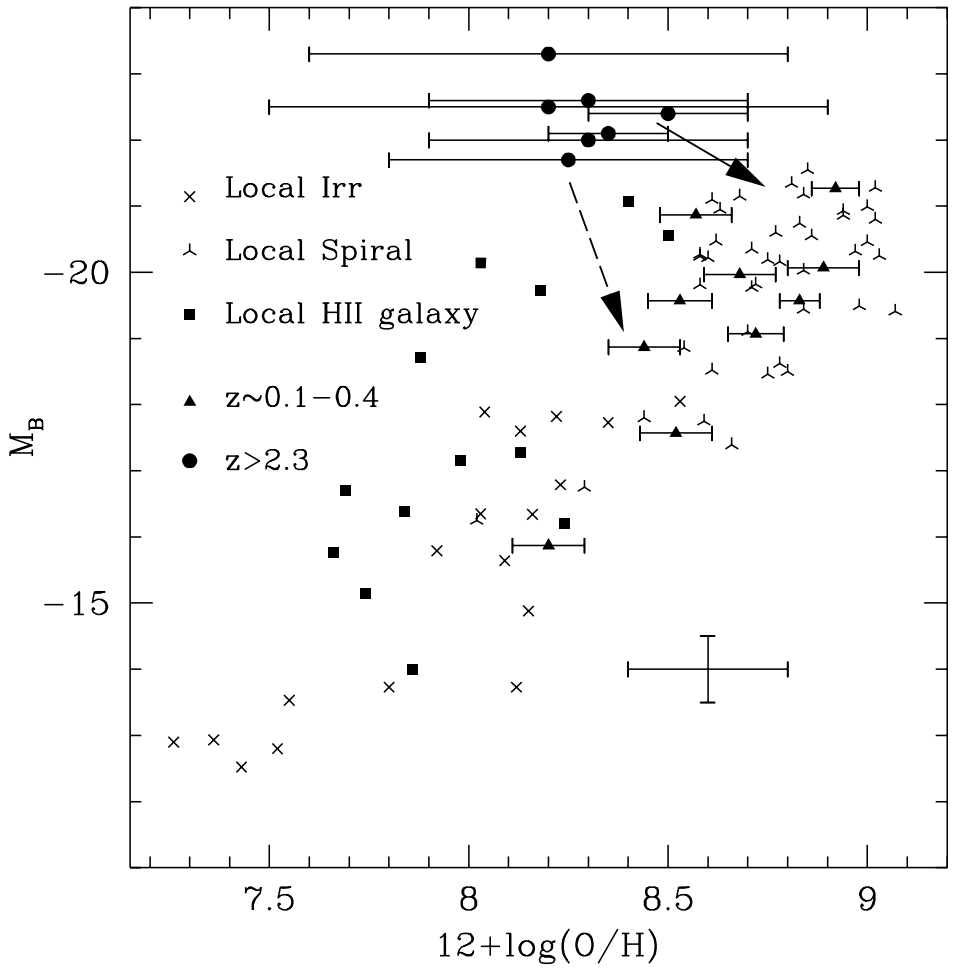

Fig. 11.— Oxygen abundance, 12+log(O/H), versus the absolute restframe B magnitude. Local irregular and spiral galaxies collected from the literature and Kobulnicky, Kennicutt, & Pizagno (1999) appear as small skeletal symbols. A representative error bar appears in the lower right. The sample of intermediate-redshift $z \sim 0.4$ emission line galaxies from Kobulnicky & Zaritsky (1999) appears as solid triangles. Solid squares denote local H II galaxies from the sample of Telles & Terlevich (1997; magnitudes corrected to the adopted cosmology). High-redshift objects from Table 4 appear as filled circles with error bars. They are significantly more luminous for their metallicity than local objects. Under the assumption that Lyman-drop galaxies evolve into modern day ellipticals and galactic spheroids, arrows indicate the tracks of high-redshift galaxies as they fade and become more chemically enriched. The solid arrow shows qualitatively the path of a galaxy which fades as its interstellar medium becomes more chemically rich by the continued cycles of star formation and metal production. The dashed line shows qualitatively the evolutionary path if continued infall of metal-poor gas is a large effect as fading proceeds.

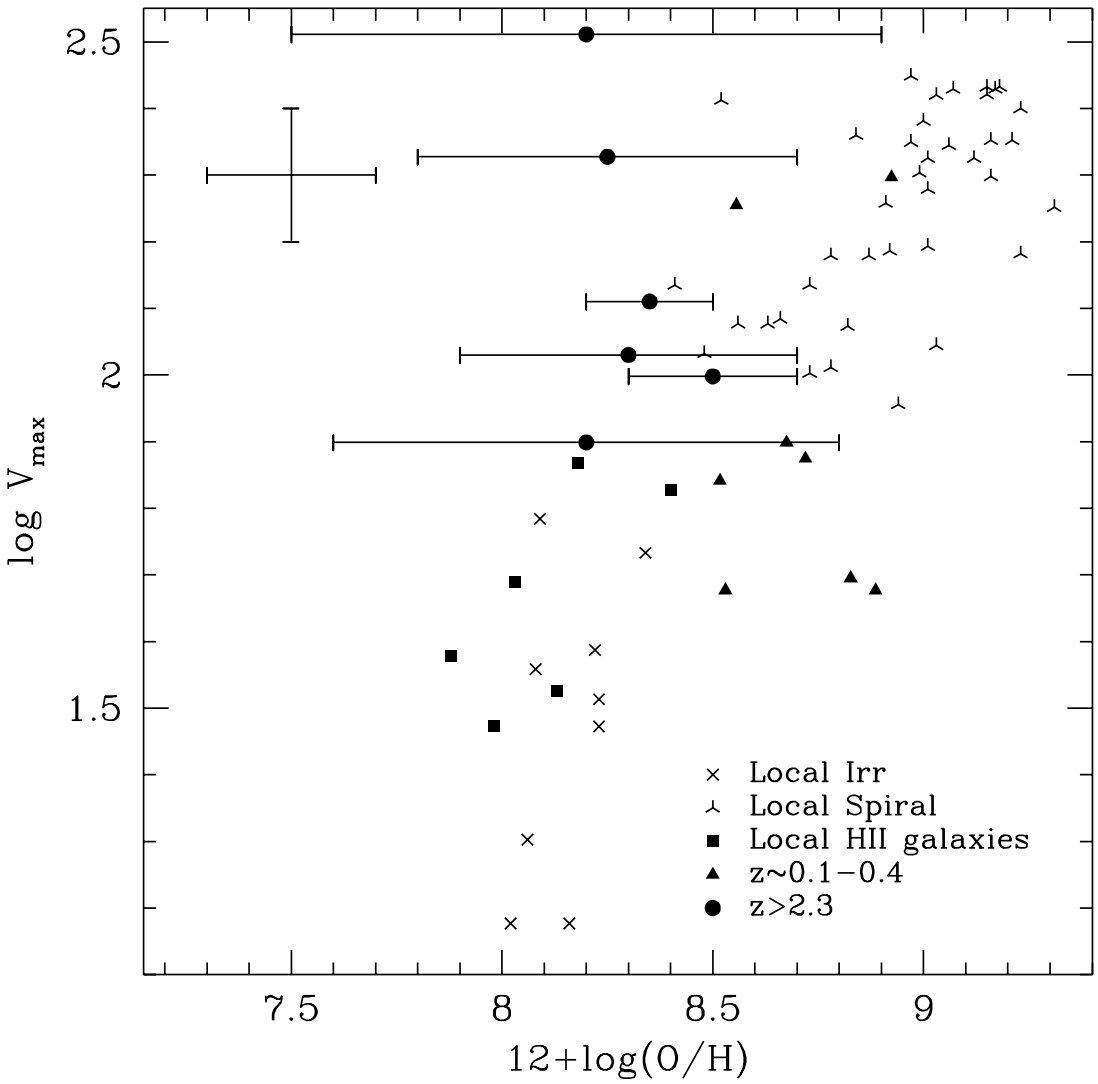

Fig. 12.— Oxygen abundance, 12+log(O/H), versus velocity dispersion, σ_v. A representative error bar appears in the lower right. Symbols are the same as in Figure 11. Kinematic widths for local spiral and irregular galaxies, corrected for inclination, come from single-dish 21-cm measurements. Kinematic widths for the high and intermediate redshift sample and for H II galaxies from Telles et al. (1997) are measured from Balmer lines with no inclination correction applied, and thus, strictly speaking, are lower limits. The $z \sim 3$ data are marginally consistent with the local metallicity-linewidth relation. Note that HII galaxies and the $z \sim 3$ sample show better agreement with local spirals and irregulars than in Figure 10.

Table 1. Target Objects

Name	CFg	Comment	Lynx 2-9691	Comment
RA (2000)	01 03 08.43	A	08 43 31.88	B
DEC (2000)	+13 16 39.6	A	+44 44 31.2	B
Redshift (z)	2.3128	A	2.8877	B
B_J[1]	...	...	23.88	B
R_F[1]	...	...	23.04	B
I_{814}	23.85	A	...	...
V_{555}	24.14	A	...	...
$r_{hl}(kpc)$	5.7	A	15	C

References. — (A) Roche et. al 2000; (B) This paper; (C) This is the radius of the [O III] emission reported here.

[1]Photographic magnitudes on the optical JK system of Kron (1980). See also Munn et al. (1997).

Table 2. Keck II NIRSPEC Observations

Name	CFgA	Lynx 2-9691
Filter for [O II]	J	N4
observed λ (Å)	11370-13960	12870-15650
rest λ (Å)	3432-4214	3310-4025
Exposure (s)	3x600	2x900
Airmass	1.55	1.12
Filter for Hβ, [O III]	H	N6
observed λ (Å)	15100-17900	17460-21600
rest λ (Å)	4558-5403	4491-5556
Exposure (s)	5x600	3x900
Airmass	1.35	1.25
Filter for Hα	K	N7
observed λ (Å)	19280-23480	23300-26900
rest λ (Å)	5820-7087	5993-6919
Exposure (s)	2x900	5x450
Airmass	1.20	1.30

Table 3. Spectral Measurements

Emission Line Fluxes	CFg	Comment	Lynx 2-9691	Comment
Lyα				
F ($\times 10^{-16}$ $erg\ s^{-1}\ cm^{-2}$)	5.6	A	1.35±0.08	B
EW (rest frame)	140	A	18±2	B
FWHM (Å) (observed)	9.4	A	14.8	B
[$O\ II$] λ3727				
F ($\times 10^{-16}$ $erg\ s^{-1}\ cm^{-2}$)	<0.47	C	<0.50	C
FWHM (Å) (observed)	...	...	...	...
Hβ λ4861				
F ($\times 10^{-16}$ $erg\ s^{-1}\ cm^{-2}$)	0.61	E	0.50±0.17	B
FWHM (Å) (observed)	...	...	10.1	B
[$O\ III$] λ4959				
F ($\times 10^{-16}$ $erg\ s^{-1}\ cm^{-2}$)	1.41±0.10	B	0.76	D
FWHM (Å) (observed)	9.5	B	...	...
[$O\ III$] λ5007				
F ($\times 10^{-16}$ $erg\ s^{-1}\ cm^{-2}$)	2.81±0.13	B	2.21±0.09	B
FWHM (Å) (observed)	16.3	B	16.9	B
Hα λ6563				
F ($\times 10^{-16}$ $erg\ s^{-1}\ cm^{-2}$)	1.65±0.07	B	1.43	G
FWHM (Å) (observed)	25.6	B	...	...
$L_{H\alpha}$ ($\times 10^{40}$ $erg\ s^{-1}$)	665	F	1250	G
SFR_{Balmer} ($M_\odot\ yr^{-1}$)	59	H	111	H
W_{FWHM} ($km\ s^{-1}$)	301	I	156	J
$\sigma = FWHM/2.35$ ($km\ s^{-1}$)	128	I	66	J
M_{vir} ($10^{10}\ M_\odot$)	7.0	K	5.2	K
F_{1500} ($\times 10^{-17}$ $erg\ s^{-1}\ cm^{-2}$ Å^{-1})	0.25	M	0.15	M
L_{1500} ($\times 10^{41}$ $erg\ s^{-1}$ Å^{-1})	3.3	L	4.3	L
SFR_{1500} ($M_\odot\ yr^{-1}$)	31	M	41	M

References. — (A) From Lowenthal et. al (1991); (B) Measurement by Gaussian fit; (C) 3σ upper limit; (D) Assuming $F_{5007}/2.9$; (E) Assuming no extinction and $F_{H\beta} = F_{H\alpha}/2.86$; (F) From the observed $H\alpha$ flux and the adopted cosmology; (G) From the observed $H\beta$ flux assuming no extinction, $F_{H\alpha} = F_{H\beta} \times 2.86 = 1.4 \times 10^{-16}\ erg\ s^{-1}\ cm^{-2}$; (H) $SFR(M_\odot\ yr^{-1}) = 8.9 \times 10^{-42}\ L_{H\alpha}\ (erg\ s^{-1})$, Kennicutt (1983); (I) Intrinsic FWHM of $H\alpha$ after correction for the instrumental profile, modeled as a Gaussian with FWHM=13.4 Å; (J) Intrinsic FWHM of [O III] λ5007 after correction for the instrumental profile, modeled as a Gaussian with FWHM=13.6 Å; (K) Virial mass estimates; see text for cautionary notes. As a fiducial size for Lynx 2-9691, we use one half of the spatial extent of the [O III] emission, 14 kpc. (L) The specific UV continuum flux and luminosity from Lowenthal et al. (1991) and our Keck/LRIS spectra. (M) Star formation rate as determined from the 1500 Å specific luminosity adopting the prescription of Madau, Pozzetti, & Dickinson

Table 4. Properties of High-Redshift Star Forming Objects

Object	log(R_{23}) (1)	$log(O_{32})$ (2)	log(O/H) +12 (3)	Ref. (4)	K_{AB} (5)	M_B (6)	Ref. (7)	z (8)	SFR (9)
CFg	> 0.86	>0.95	$7.8 - 8.7$	A	23.1	-21.6	G	2.313	59
Lynx 2-9691	0.70-1.02	>0.77	$8.3 - 8.8$	A	22.7	-22.5	H	2.888	111
MS1512-cB58	0.92	0.17	$8.2 - 8.5$	B	23.0	-22.1	I	2.739	21
Q0201+113 C6	>0.83	···	$7.9 - 8.7$	C,D	23.4	-22.0	J	3.053	85
DSF2237+116 C2	>0.65	···	$7.6 - 8.8$	C,E	22.3	-23.3	J	3.333	276
B0902+343 C6	>0.56	···	$7.5 - 8.9$	C	22.9	-22.5	J	3.099	53
Westphal CC13	>0.63	···	$7.6 - 8.8$	F	23.1	-22.5	K	3.406	39

References. — (1) Emission line ratio $R_{23} = (F_{4959} + F_{5007} + F_{3727})/(F_{H\beta})$; (2) Ionization parameter ratio $O_{32} = (F_{5007} + F_{4959})/F_{3727}$; (3) Oxygen abundance relative to hydrogen; (4) Reference; (5) K_{AB} magnitude; (6) Rest frame blue magnitude on the Vega system for comparison to local galaxies, computed as described in Column 7; (7) Reference for photometry; (8) Redshift; (9) Star formation rates, from either the Balmer recombination line luminosities for objects presented here, or from [O III] line luminosities as tabulated by Teplitz et al. (2000a)
(A) This work; (B) Teplitz et al. (2000a); (C) Pettini et al. (1998); (D) $[O\ III]$ λ5007 is not observed due to night sky line contamination; assume $F_{5007} = 2.9F_{4959}$; (E) $[O\ III]$ λ4959 not observed due to night sky line contamination; assume $F_{4959} = F_{5007}/2.9$. (F) Teplitz et. al 2000b; (G) Computed using the observed $V_{AB} \simeq V_{555} = 24.14$ from Roche et al. (2000), assuming the same color as MS1512-cB58 ($V_{AB} - K_{AB} = 1.0$) (Ellingson et al. 1996) to obtain the K_{AB} listed in column 6. The distance modulus of 46.4 mag and bandpass term of the K correction, -2.5log(1+z)=1.3, yields $M_{R\ AB} = -22.0$. Assuming $(B - R_C)_{AB} = 0.4$ for an Im type SED (Fukugita et al. 1995), yields the final restframe B-band estimate of -21.6. (H) Computed from the measured photographic magnitude of $R_F = 23.04$, assuming $R_F - R_{AB} \sim -0.1$ and the same $R_{AB} - K_{AB} = 0.4$ color as a similar high-redshift object 0000-263 D6 from Pettini et al. (1998) yields $K_{AB} = 22.7$. A distance modulus of 47.0 mag, with the bandpass term of the K correction -2.5log(1+z)=1.5 mag for $z = 2.9$, yields a rest-frame $M_{V\ AB}$ of -22.8. Adopting $B - V$=0.27 for an Im type SED (Fukugita et al. 1995) suggests a final rest-frame M_B of -22.5; (I) Corrected for gravitational magnification (Seitz et al. 1998) who give $R = 23.9$ and $K_{AB} = 23.0$ after demagnification. Applying a distance modulus of 46.8 mag, a K correction bandpass term of 1.4 mag, and assuming B-V=0.27 for an Im type spectral energy distribution (Fukugita et al. 1995) yields the final rest-frame B magnitude of -22.1; (J) Computed assuming that the observed K_{AB} magnitude from Pettini et al. (1996) is approximately the rest frame V magnitude, adopting B-V=0.27 for an Im type spectral energy distribution (Fukugita et al. 1995), a K correction of 1.5 mag (1.6 mag for Westphal CC13) , and the appropriate distance modulus; (K) Computed assuming that the observed K_{AB} magnitude from Teplitz et al. (2000a) is approximately the rest frame V magnitude, adopting B-V=0.27 for an Im type spectral energy distribution (Fukugita et al. 1995), a K correction of 1.5 mag, and the appropriate distance modulus.

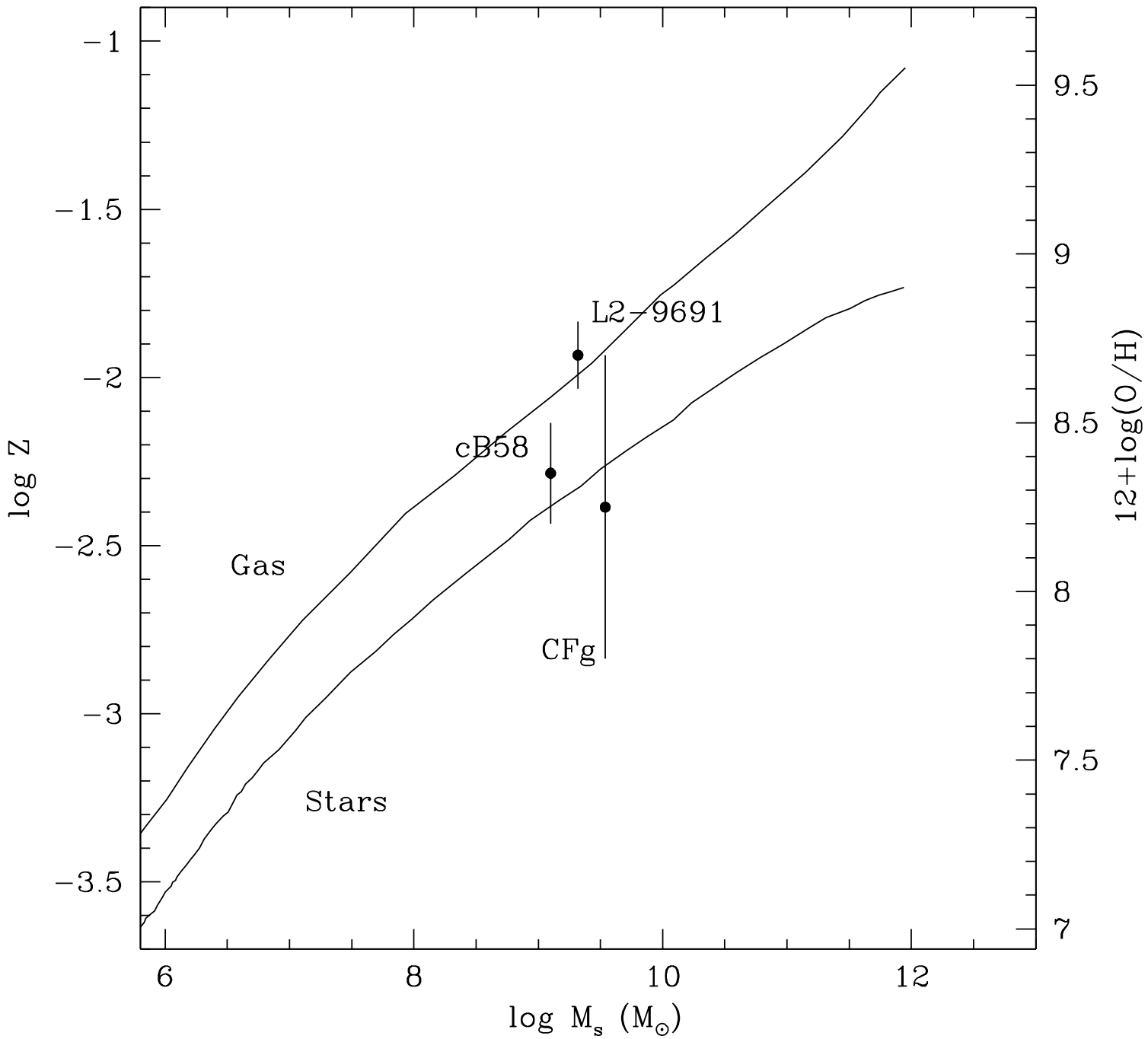
−1
−1.5
−2
−2.5
−3
−3.5
log Z
9.5
9
8.5
8
7.5
7
12+log(O/H)
6
8
10
12
log M$_s$ (M$_\odot$)
L2−9691
cB58
CFg
Gas
Stars